Ergodic Properties of Triangular Billiards: A Numerical Study

by

Katerina Zahradova

Submitted in partial fulfillment of the requirements of the Degree of
Doctor of Philosophy

School of Mathematical Sciences
Queen Mary, University of London
United Kingdom

June 2022

Declaration

I, Katerina Zahradova, confirm that the research included within this thesis is my own work or that where it has been carried out in collaboration with, or supported by others, that this is duly acknowledged below and my contribution indicated. Previously published material is also acknowledged below.

I attest that I have exercised reasonable care to ensure that the work is original, and does not to the best of my knowledge break any UK law, infringe any third party's copyright or other Intellectual Property Right, or contain any confidential material.

I accept that the College has the right to use plagiarism detection software to check the electronic version of the thesis.

I confirm that this thesis has not been previously submitted for the award of a degree by this or any other university.

The copyright of this thesis rests with the author and no quotation from it or information derived from it may be published without the prior written consent of the author.

Signature:

Date:

Details of collaboration and publications:

Parts of this work have been completed in collaboration with Dr. Oscar Bandtlow, Dr. Wolfram Just, and Dr. Julia Slipantschuk and are published in the following paper:

Impact of symmetry on ergodic properties of triangular billiards Zahradova, K., Slipantschuk, J., Bandtlow, O. F., Just, W., Physical Review E, 105 (2022)

Abstract

Polygonal billiards represent one of the simplest examples of systems with anomalous dynamics. So far, they have resisted numerous attempts to fully describe their dynamical behaviour. There is still a lack of complete understanding of even some basic features, such as ergodicity or the decay of correlations. In this thesis, we study the dynamical properties of triangular billiards using numerical means. We highlight the importance of the billiard table geometry, more specifically symmetry, for the resulting dynamics. We show that while typical triangular billiards appear to show correlation decay as expected by the community, symmetric billiards may not even be ergodic with respect to the uniform distribution in phase space. We provide compelling evidence that symmetry plays a decisive role in the dynamics. We further show that the relation between dynamical properties of symmetric and right-angled triangular billiards shows a rich interplay.

Acknowledgments

First and foremost, my deepest thanks belong to my supervisors, Oscar Bandtlow and Wolfram Just, for making the last almost four years an exciting adventure as well as making them possible in the first place. There are many things I would like to thank Oscar for, so I will name just a few: for teaching me so much and treating me like a young colleague, for allowing me to highjack the research away from estimating integrals, and lately for his endless patience with all my missing or redundant articles. I would like to thank Wolfram for his unending optimism and support, many physics-y insights, and all the long insightful emails. I would also like to thank Julia for sharing her coding expertise and being there for me. My thanks belong to all three of them for helping me and guiding me on this adventure. I am grateful for the financial support from the Faculty of Sciences and Engineering and the School of Mathematical Sciences.

I want to thank Honza for his unwavering love and support, crazy ideas, and just for being there for me through this journey. As per his particular request, I would also like to express my immense gratitude for him mowing the lawn that one weekend when I was writing this thesis.

I am very grateful to my friends, both in London and otherwise, for the lunch breaks, coffee breaks, lockdown Zoom game nights, and all the weird and fascinating discussions. A special thanks belong to Jasna and Maldon - getting to know you both have made the last four years very special to me.

My sincerest thanks go to my parents and my family for their endless love and support. I wouldn't be here without you.

Notation and Abbreviations

GM	an angle of $\pi(\sqrt{5}-1)/4$
SM	an angle of $\pi(\sqrt{2}-1)/4$
PiPi	an angle of $\pi^2/8$
SQ2	an angle of $\pi\sqrt{2}/4$
SQ3	an angle of $\pi\sqrt{3}/4$
Log3	an angle of $\pi \log 3/2$
Pi2	an angle of $\pi/2$
Pi4	an angle of $\pi/4$
Pi3	an angle of $\pi/3$
Leb.	Lebesgue measure
FFT	Fast Fourier Transform
N	total number of collisions, index n used in sums
M	number of cuts/initial conditions
α, β	defining angles of a triangular billiard
L	circumference of a triangular billiard

For the reader's convenience, we also include the following estimates:

2^{20}	$\approx 10^6$
2^{23}	$\approx 8 \times 10^6$
2^{27}	$\approx 10^8$
2^{30}	$\approx 10^9$

Table of Contents

Introduction

Complex dynamical systems attract a considerable amount of research interest. This is not altogether surprising as this interesting field sits at the juncture of mathematics, physics, and their real-world applications. There is a huge body of knowledge pertaining to the complex chaotic behaviour, see *e.g.*, [5, 8, 17, 19]. While the main mechanisms for chaotic behaviour such as sensitivity, hyperbolicity, correlation decay, and others have been identified, many open problems still remain. A next possible target could be in anomalous dynamics, a field consisting of systems without uniform hyperbolicity and without exponential decay of correlation, see *e.g.* [20, 33] for typical references covering a wide range from rigorous mathematical approaches to real world applications.

Billiard dynamics, broadly understood as the geodesic flow on a Riemannian manifold with a boundary and possibly also with corners and other singularities, lends itself extremely well to simulating numerous physical systems, both in a realistic and a simplified perspective. In this thesis we focus our attention on planar billiards, which are characterised by the movement of a point particle in a subset of $\mathbb{R}^2$. More specifically, we shall discuss polygonal billiards, the two dimensional ballistic motion of a point particle moving within a polygonal domain with elastic collisions at the boundary. These billiards constitute one of the simplest examples of systems with anomalous dynamics [23]. While there is no apparent mechanism responsible for irregular motion, their dynamics is more complicated than it might seem.

The study of ergodic properties of billiards has been a fruitful area of research. The

geometrical shape of the underlying billiard table determines the qualitative properties of the system. According to [23], we can divide planar billiards into three main classes as follows. Firstly, there are billiards with smooth and strictly convex walls, initially investigated in [6] and termed elliptic in [23]. The second class is constituted by billiards with piecewise concave and piecewise smooth boundaries (see *e.g.* [9, 14]). The dynamics of these billiards is hyperbolic. Lastly, the third class are billiards where the underlying table is a polygon and the corresponding dynamics is parabolic, see *e.g.* [21, 22]. There are several different ways of studying the dynamical behaviour of billiards. One might study the billiard flow [32, 51], the billiard map or an induced map (see *e.g.* [10]), or one might study a simplification of the system, such as the triangular map considered in [11, 26]. A different approach to studying billiard dynamics amounts to replacing the classical Hamiltonian with the stationary-state Schrödinger equation with Dirichlet boundary conditions, see *e.g.* [37, 40]. These billiards are called quantum billiards.

In this thesis, we shall focus on the polygonal class, which can be further divided into two cases. The first one consists of rational polygonal billiards, which have all angles of the billiard table commensurable with π, while the second one encompasses irrational polygonal billiards, where at least one angle is an irrational multiple of π. There are more results in the literature for the rational case, as the number of scattering angles occurring for a given orbit in rational polygonal billiards is finite and the phase space foliates into invariant sets which consists of collections of lines. The dynamics on these invariant lines can be captured by one-dimensional piecewise linear invertible maps, known as interval exchange transformations, which can be studied rigorously. Fairly accessible reviews are available, see *e.g.* [22, 38, 49]. Overall, this device, namely the reduction to interval exchange transformations, makes it possible to develop computable criteria for various dynamical properties such as minimality [30], ergodicity [7], or weak mixing [44]. On the other hand, a seminal result [29] excludes the possibility of (strong) mixing. In this context a set of polygonal billiards which are weakly mixing has been described in [24]. Maybe the only result concerning 'typical' polygonal billiards and ergodicity of Lebesgue

measure is [32], where the authors used sophisticated approximations of general polygons by rational polygons. A constructive example can be found in [50].

Alongside and complimenting these rigorous claims are results of numerical simulations, usually found in the physics literature and focusing on irrational polygonal billiards, see *e.g.* [1, 10]. Numerical results suggest that irrational billiards are ergodic with respect to the Lebesgue measure, in agreement with rigorous claims [12]. In some cases, correlation decay indicates weak and even strong mixing [11, 26]. However, numerical results are not always conclusive [42, 53].

Let us now focus solely on the subject of triangular billiards. Again, even basic properties like the existence of dense orbits are hard to prove [41]. We can divide triangular billiards into three groups as follows. Firstly, we have rational triangular billiards. The dynamics in these triangles is not ergodic, it is in fact pseudointegrable [22]. Interesting facts about lattice polygons, introduced in [48] are investigated in [31] and [39]. Next there are triangular billiards where exactly one angle is a rational multiple of π, such as typical right-angled triangular billiards. These have been extensively studied, with somewhat mixed results. Some authors claim weak (but not strong) mixing [2], some claim non-ergodicity [53], extremely slow logarithmic diffusion [27], and [42] even argues for ergodicity in spite of [53]. Lastly, we have (fully) irrational triangular billiards, with all angles irrational multiples of π. Numerical simulations indicate that they are ergodic and mixing [10].

The popularity of triangular billiards stems not only from the triangle being the simplest polygon resulting in a non-trivial dynamics but also from the fact that the dynamics in triangular billiards can model particle collisions in different settings. More specifically, the dynamics in a right-angled triangular billiard corresponds to a system of two elastic hard-point masses moving between hard walls [15], whereas the dynamics in a generic acute triangular billiard is equivalent to the motion of three point-like particles on a ring. In all these cases, the masses of the particles relate to the angles of the corresponding triangular billiard.

In this thesis, we mainly focus on numerically investigating ergodic properties of irrational triangular billiards by approximating them using rational triangular billiards. We are interested in the ergodicity of Lebesgue measure, partly as the uniform distribution is the natural candidate and also due to results of [32], that assert ergodicity of Lebesgue measure for a large set of irrational triangular billiards. Again, deriving analytical results is intrinsically very difficult, which explains why most concrete results are numerical in nature. However, as mentioned earlier, some of the reported results contradict each other. Moreover, authors rarely properly explain how they carried out their simulations, making reproducing their results nearly impossible. In this thesis, we aspire to make our numerical simulations transparent and easily reproducible by including a chapter documenting the algorithms we used as well as by making the code public. As we demonstrate later in the thesis, some quantities show considerable dependence on the method of their calculation, making this transparency all the more important.

While most results in the literature, see *e.g.* [53], claim that changes in irrationality of the angles of the billiard table are the leading cause for changes in the dynamical behaviour, a counterargument, presented in [36], asserts that geometry is more important. The authors of [36] have studied a one parameter family of irrational triangular billiards, defined by setting the lengths of the sides of the table be consecutive integers $(N, N+1, N+2)$ for $N \in [3, \infty)$, using results of [16, 47]. Their results imply that geometry is dictating the change in the dynamics.

Although we do not study triangular billiards constructed in this fashion, we shall present results reinforcing that geometry, or rather symmetry, is the key factor in the ergodic behaviour of triangular billiards. In all our simulations, number theoretic properties of angles in the billiard do not play a qualitative role. Somewhat surprisingly the deciding factor for the dynamical behaviour is whether the investigated triangular table is *symmetric*, *i.e.* isosceles, or *asymmetric*. We present numerical results suggesting that while asymmetric triangular billiards seem to be mixing, in line with results in the literature [10], their symmetric counterparts exhibit behaviour which suggests non-ergodicity

of Lebesgue measure.

The organisation of this thesis is as follows. Chapter 1 covers the necessary mathematical background, including the billiard map for triangular billiards and an overview of some important facts about ergodicity and mixing. We also clarify how we define the triangular billiards used in our computations. Chapter 2 outlines algorithms used in the numerical computations. We provide an explanation and justification for the methods of computation of autocorrelation functions as our simulations indicate that some cases of triangular billiards exhibit considerable dependence on the method used in the calculation of autocorrelations. A brief excursion into rational triangular billiards can be found in Chapter 3. We discuss phase portraits, an unfolding of a particular example of an almost integrable rational billiard, and examine the dynamical behaviour of rational approximations of irrational triangular billiards. Results pertaining to asymmetric irrational billiards are in Chapter 4. Outcomes of our simulations confirm the belief found in the literature that asymmetric irrational billiards are mixing. The effects of changing time scales and ensemble sizes are investigated in order to ensure that our conclusions do not paint an incomplete picture. In our investigation, we discovered that symmetric triangular billiards exhibit different dynamical behaviour to that of their asymmetric counterparts. We present results of several different numerical tests, showcasing the effects of symmetry and its breaking, in Chapter 5. Chapter 6 discusses right-angled triangular billiards. While the right-angled and symmetric billiards are closely related by the process of unfolding, this does not fully translate to their dynamics. Additionally, we present results indicating that the rich dynamical behaviour of the right-angled case does not seem to stem from the fact that the right angle is a rational multiple of π by comparing their behaviour to other irrational triangular billiards with one angle commensurable with π. Finally, the last chapter, Chapter 7, focuses on so-called *thin* triangular billiards. We take inspiration from the only explicit example, [50], where the author proves ergodicity of Lebesgue measure for a triangular billiard constructed in a particular way using Liouville numbers. The study of triangular billiards where at least

one angle of the table is small provides us with further opportunities to study the effects of symmetry.

Chapter 1

Mathematical background

The purpose of this chapter is to provide an introduction to triangular billiards. We start with the slightly broader topic of polygonal billiards, and then focus on the triangular case. This chapter is based on [14, 38, 52].

The outline of this chapter is as follows. In Section 1.1 we introduce and explain polygonal billiards, along with the coordinates used, the map used to model the dynamics and we briefly discuss why we chose to focus on the map instead of the flow. An explanation of ergodicity and mixing is given in Section 1.2. In Section 1.3, the different observables we use to determine ergodicity and mixing are discussed. Lastly, the various angles and triangles, along with the notation, are summarised in Section 1.4.

1.1 Polygonal billiards

Firstly, we define the broader notion of polygonal billiards, before specialising on the triangular case. We are mainly following [14].

Definition 1.1. Let $\mathcal{D} \subset \mathbb{R}^2$ be a compact polygon. A *polygonal billiard system* corresponds to the free motion of a point particle inside of $\mathcal{D}$ with specular reflection at the boundary $\partial\mathcal{D}$.

Remark. In general, $\mathcal{D}$ does not have to be convex or simply connected. However, we shall assume both.

Notation 1.1. The boundary $\partial\mathcal{D}$ is a finite union of closed line segments Γ_i,

$$\partial\mathcal{D} = \Gamma = \Gamma_1 \cup \cdots \cup \Gamma_r,$$

where r is the number of vertices of $\mathcal{D}$. We refer to $\mathcal{D}$ as the *billiard table* and $\Gamma_1, \ldots, \Gamma_r$ the *walls*. We call $x \in \mathcal{D}$ a *corner point* if $x \in \Gamma_* = \partial\Gamma_1 \cup \cdots \cup \partial\Gamma_r$, and a *regular boundary* point if $x \in \tilde{\Gamma} = \Gamma \setminus \Gamma_*$. We also fix an orientation of each Γ_i by requiring that $\mathcal{D}$ be to the left.

Now we can construct the dynamics on a billiard table. Let $q \in \mathcal{D}$ denote the position of the moving particle and $v \in \mathbb{R}^2$ its velocity vector. Both are functions of time $t \in \mathbb{R}$, *i.e.* $q = q(t)$ and $v = v(t)$. While the particle moves inside the table, its velocity is constant:

$$\dot{q} = v \quad \text{and} \quad \dot{v} = 0 \quad \text{for } q \in \operatorname{int}(\mathcal{D}), \tag{1.1}$$

where dot denotes the time derivative.

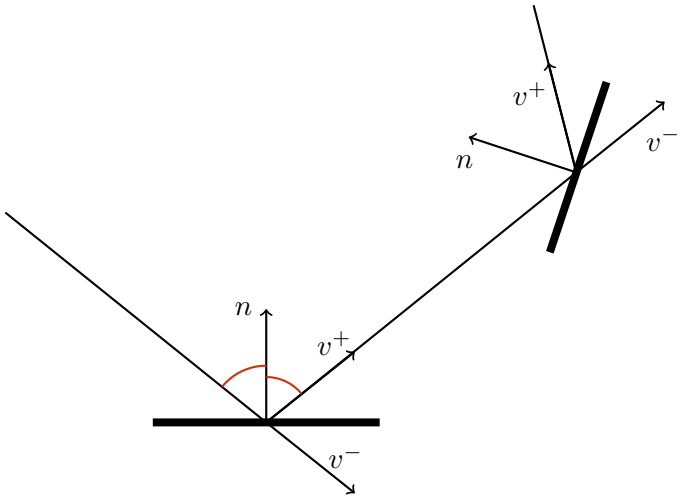

Figure 1.1: Velocity vector change at collision.

When the particle collides with the regular part of the boundary $\tilde{\Gamma}$, its velocity vector

is instantaneously reflected along the inner normal vector to Γ at q. This corresponds to the classical rule 'the angle of incidence is equal to the angle of reflection', see Figure 1.1, and can be represented by

$$v^+ = v^- - 2\langle v, n\rangle n, \tag{1.2}$$

where v^+ and v^- refer to velocities after and before collision respectively, and n denotes the inward facing normal to $\tilde{\Gamma}$ at the point q. If the moving particle hits a corner point, *i.e.* $q \in \Gamma_*$, it stops and the motion will no longer be defined beyond this point as there is not a unique way to reflect it. This is one of the facts complicating the study of polygonal billiards.

As the equations (1.1) and (1.2) preserve the Euclidean norm of $\|v\|$, we consider a particle moving with unit speed, $\|v\| = 1$.

The following lemma ([14, p.24]) answers the question whether a particle can spend an infinite time being 'trapped' by a corner. We shall revisit it in Chapter 7.

Lemma 1.1. If a particle enters a neighbourhood of a corner in a polygonal billiard with an angle $\gamma > 0$ and collides with both walls adjacent to the corner, it must leave that neighbourhood after at most $\lfloor \pi/\gamma \rfloor$ collisions.

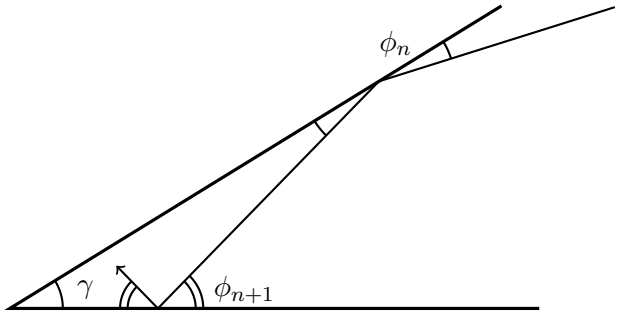

Figure 1.2: Proof of Lemma 1.1.

Proof. As walls of the corner are flat, it is easy to check that the angles of incidence/reflection grow as $\phi_{n+1} = \phi_n + \gamma$, see Figure 1.2. Therefore, after $\lfloor \pi/\gamma \rfloor := m$ collisions, $\phi_m > \pi$ as $\phi_0 > 0$. Thus, the particle needs to leave the neighbourhood of the corner. □

Remark. Lemma 1.1 also demonstrates that in order for a particle to hit the corner point, the immediate collision beforehand cannot be with one of the adjacent sides as that would mean $\phi_n = 0$.

The state of the moving particle at any time is uniquely specified by its position $q \in \mathcal{D}$ and the unit velocity vector $v \in S^1$. The *phase space* of the system is

$$\Omega = \{(q, v)\} = \mathcal{D} \times S^1 \,,$$

a three-dimensional manifold with boundary $\partial\Omega = \Gamma \times S^1$. Visually, Ω can be imagined as a 'doughnut' with $\mathcal{D}$ as its cross-section.

We can also identify the collision pairs (q, v^-) and (q, v^+) for all regular boundary points $q \in \tilde{\Gamma}$, effectively 'glueing' Ω along its boundary. The natural projections of Ω onto $\mathcal{D}$ and S^1 are denoted by π_q and π_v, so that $\pi_q(q, v) = q$ and $\pi_v(q, v) = v$.

Let $\tilde{\Omega} \subset \Omega$ denote the set of states (q, v) for which the dynamics of the moving particle is defined for all times $-\infty < t < \infty$. We get a one-parameter group of transformations

$$\Psi^g : \tilde{\Omega} \to \tilde{\Omega}$$

with continuous time $g \in \mathbb{R}$, which we call the *flow*. The flow satisfies the following: $\Psi^0 = \mathrm{id}$ and $\Psi^{g+h} = \Psi^g \circ \Psi^h$ for all $g, h \in \mathbb{R}$. Every trajectory of the flow $\{\Psi^g x\}, x \in \tilde{\Omega}$ is a continuous curve in Ω thanks to the identification of v^- and v^+. The projection $\pi_q(\Psi^g x)$ onto the table $\mathcal{D}$ is called a billiard trajectory. It consists of a directed polygonal line the vertices of which are points of collision on the boundary.

Although many results in the literature focus on investigating the billiard dynamics with regards to the flow, we chose to study the collision map instead. Our interest stems from a project investigating approximations of transfer operators associated with triangular billiards and their application in industry [13, 45, 46] which use the map as it is an easier object to study than a flow.

One can reduce the flow to a map by constructing a cross-section. Given a flow $\Psi^u : \Omega \to \Omega$ on a manifold Ω, one finds a hypersurface $M \subset \Omega$ transversal to the flow so that each trajectory crosses M infinitely many times. Then the flow induces a return map $F : M \to M$ and a return time function $L(x) = \min\{u > 0 | \Psi^u(x) \in M\}$ on M, so that $F(x) = \Psi^{L(x)}(x)$.

For a billiard table, this hypersurface M is usually constructed on the boundary of the billiard table, *i.e.* on the set $\Gamma \times S^1$. Due to our previous identification of v^- and v^+, it is customary to describe the cross-section as the set of all velocities *after* collision, *i.e.* v^+:

$$\mathcal{M} = \cup_i \mathcal{M}_i, \quad \mathcal{M}_i = \{x = (q, v) \in \Omega \,|\, q \in \Gamma_i, \langle v, n\rangle \geq 0\}, \tag{1.3}$$

where n denotes the unit normal vector to Γ_i pointing inside $\mathcal{D}$. The set $\mathcal{M}$ is a two-dimensional submanifold in Ω called the *collision space*.

Remark. Let $x = (q, v) \in \mathcal{M}_i$. Then the trajectory $\Psi^g x$ is defined for some small interval $0 < g < \varepsilon$ when q is a regular boundary point ($q \in \tilde{\Gamma}$) with $\langle v, n\rangle > 0$.

If the trajectory $\Psi^g x$ for $x \in \mathcal{M}$ is defined during some interval of time $(0, \varepsilon)$, then it can be shown that it will intersect the surface $\Gamma \times S^1$ at a future time $\tau(x) > 0$, and we call $\tau(x)$ the *return time*. Since the particle has unit speed, the return time $\tau(x)$ will be equal to the distance between the two subsequent collisions with the boundary.

Any trajectory of the flow $\Psi^g : \tilde{\Omega} \to \tilde{\Omega}$ crosses the surface $\mathcal{M}$ infinitely many times. Let $\tilde{\mathcal{M}} = \mathcal{M} \cap \tilde{\Omega}$. We define the *return map* $\mathcal{T}$ as

$$\mathcal{T} : \tilde{\mathcal{M}} \to \tilde{\mathcal{M}}, \quad \mathcal{T}(x) = \Psi^{\tau(x)+0} x\,. \tag{1.4}$$

The map $\mathcal{T}$ is often called the *billiard map* or *collision map* and $\mathcal{M}$ is called the *phase space of the billiard map* $\mathcal{T}$.

For every point $x \in \mathrm{int}(\mathcal{M})$ its trajectory $\Psi^g x$ is defined, at least, for $0 < g < \tau(x)$, *i.e.* until the next collision with the boundary, at which there are two different

possibilities:

1. a regular collision, *i.e.* $\Psi^{\tau(x)+0}x$ is not a corner point;

2. the trajectory hits a corner point and dies.

Note that when x corresponds to a corner point there is no sensible way to define $\mathcal{T}(x)$. Therefore, while $\mathcal{T}$ can be extended beyond $\tilde{\mathcal{M}}$, we cannot extended it to the whole collision space $\mathcal{M}$. We can, however, extend it for trajectories either originating or ending in a corner point by considering only the part of the orbit from/until the corner point.

1.1.1 Triangular billiards

Among the many ways one can define and describe a triangular billiard table, we chose the following. We fix the size of one side and vary the adjacent angles. This construction allows us to study the effect of changing angles in the billiard with ease and hence make our analysis more approachable as we can conveniently talk about different configurations just using the two angles, α and β in our notation, see Figure 1.3, and we refer to the resulting billiard as the α-β triangular billiard. See Notation or Section 1.4 for a list of angles used along with their abbreviations.

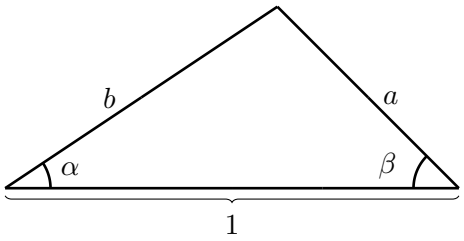

Figure 1.3: Illustration of the construction of a triangular billiard. Note our convention: the horizontal side has fixed length 1, while the adjacent angles α and β are variable. The sides a and b, as well as the remaining angle, are determined using basic trigonometry.

There are two ways of dealing with dynamics on the billiard table. One can either use normal Euclidean coordinates on the boundary viewed as a subset of $\mathbb{R}^2$, or one uses the so-called Birkhoff coordinates. Even though at first glance it might seem that using

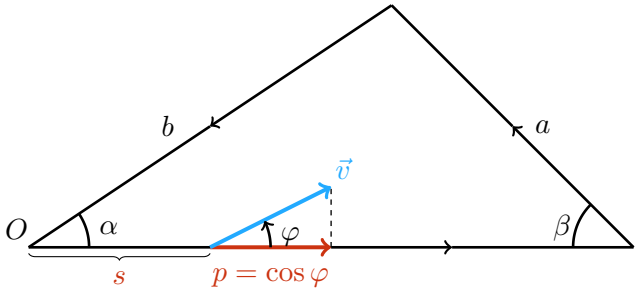

Figure 1.4: Illustration of the definition of Birkhoff coordinates (s, p) (in red). The original speed $\vec{v}$ is indicated in light blue. The origin point is denoted by O.

Euclidean coordinates is easier as one can quickly determine and visualise exact position in the billiard, the converse is true. Therefore, we will work in Birkhoff coordinates (s, p), which describe the position of our point-like particle on the boundary. They are defined as follows. We select an origin O on the boundary. In our case, we select the corner point adjacent to angle α as the origin in all calculations. The position s of the particle on the boundary is given by the distance from the origin along the boundary, measured following the orientation of the walls. Denote by $\varphi \in [0, \pi]$ the angle between the oriented boundary wall and the outward velocity vector. The momentum p is then given as $p = \cos\varphi$, *i.e.* it is the tangential velocity component. See Figure 1.4 for a visual representation.

Collision map for triangular billiards

Using Birkhoff coordinates, we can define the billiard map as

$$T(s, p) = (s', p') \tag{1.5}$$

where

$$\begin{cases} s' = s^{(1)} + (s^{(1)} - s)\frac{\sqrt{1-p^2}}{\sqrt{1-p^2}\cos\lambda + p\sin\lambda} \\ p' = \sqrt{1-p^2}\sin\lambda - p\cos\lambda \end{cases} \qquad \text{for } p \in (p_s, 1)$$

$$\begin{cases} s' = s^{(0)} - (s - s^{(0)})\frac{\sqrt{1-p^2}}{\sqrt{1-p^2}\cos\kappa - p\sin\kappa} \\ p' = -\sqrt{1-p^2}\sin\kappa - p\cos\kappa \end{cases} \qquad \text{for } p \in (-1, p_s),$$

with

$$p_s = \frac{c_s}{\sqrt{1+c_s^2}} \quad \text{and} \quad c_s = \frac{s^{(1)} - s}{s^{(2)} - s^{(1)}}\csc\lambda - \cot\lambda.$$

Values of κ, λ, $s^{(0)}$, $s^{(1)}$, and $s^{(2)}$ can be found in Table 1-A as they vary depending on which side the particle starts.

	κ	λ	$s^{(0)}$	$s^{(1)}$	$s^{(2)}$
$s \in (0,1)$	α	β	0	1	$1+a$
$s \in (1,1+a)$	β	$\pi-\alpha-\beta$	1	$1+a$	$1+a+b$
$s \in (1+a,1+a+b)$	$\pi-\alpha-\beta$	α	$1+a$	$1+a+b$	$1+a+b+1$

Table 1-A: Table summarising important angles and values for the definition of the map.

The quantity p_s introduces a line of discontinuity into the billiard map T, see Figure 1.5. The value of p_s is important as it represents a critical momentum necessary in order for the trajectory to end up in the opposite corner, given a starting position s. If $p < p_s$, the particle collides with the wall on the left, $p > p_s$ and particle collides with the wall on the right. These discontinuities are the reason why writing down the n-th iterate T^n in closed form is intrinsically very difficult.

Unfolding

Instead of considering the orbit bouncing within the triangular billiard it is sometimes simpler to use a so-called Zemlyakov Katok construction [55]. Rather than reflecting the orbit we can reflect the triangular billiard about the side of the each collision so that the trajectory becomes a straight line, see Figure 1.6. This so-called unfolding will

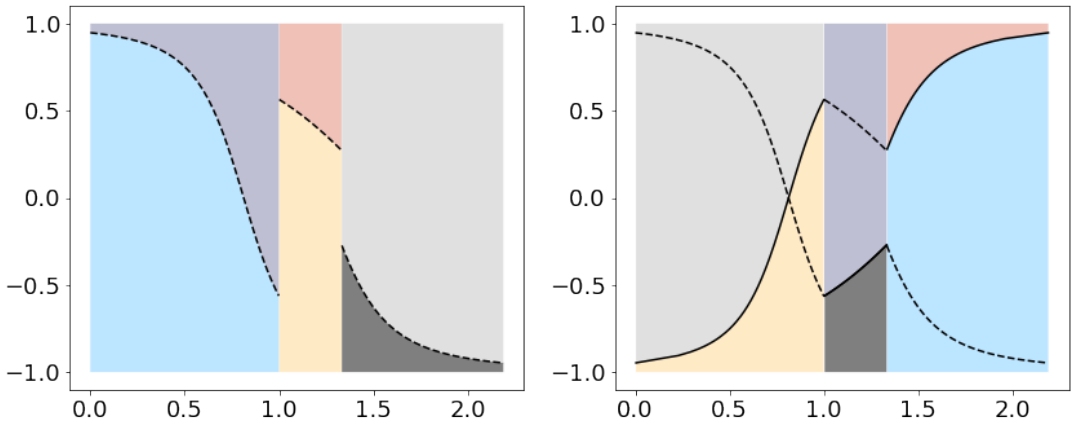

Figure 1.5: Phase space (on the left) of the SM-GM triangular billiard, divided into regions by p_s (dashed), along with the corresponding images under one iteration of the map T (right). The colours between left and right hand side match, *e.g.* the lower left light blue region maps to the lower right light blue region.

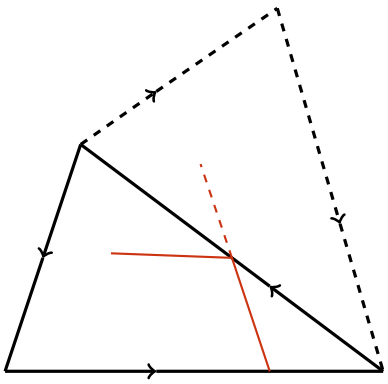

Figure 1.6: Illustration of unfolding of the triangular billiard. Normal trajectory (red, full line) and the unfolded one (red, dashed) is plotted for one collision.

then produce a complicated and potentially infinite flat surface, where the actual billiard orbits are given by straight lines. Only very few cases, which we call integrable billiards, will result in a simple topology, namely a torus. These are the equilateral triangular billiard (with all angles equal to $\pi/3$), the symmetric right-angled triangular billiard (with angles $\pi/4$, $\pi/4$, $\pi/2$), and the asymmetric right-angled triangular billiard (with angles $\pi/3$ and $\pi/6$). The unfolding of the last case is given in Figure 1.7.

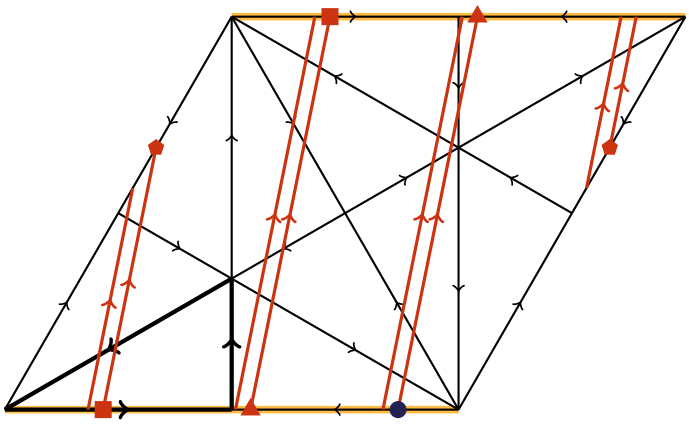

Figure 1.7: Unfolding of an integrable triangular billiard with angles $\pi/6$, $\pi/2$, $\pi/3$. The original triangular billiard is indicated by the thick outline. The opposite sides of the resulting parallelogram are identified so that the resulting flat surface is a flat torus. Two nearby orbits (originating from the dark blue circle) are shown by straight lines (solid red), with the corresponding collisions with the horizontal side identified by red geometric shapes. A potential Poincare cross section for the flow is indicated is yellow.

Classification of triangular billiards

Although the angles used in the construction of the triangular billiard do not play a qualitative role in the map, they play an important role in the dynamical properties of the billiard. We can classify them as follows:

1. *Rational triangular billiards:* all angles are rational multiples of π, *i.e.* $\alpha, \beta \in \pi\mathbb{Q}$. We further investigate their behaviour in Chapter 3.

2. One rational angle: one angle is a rational multiple of π, while the other two are irrational multiples of π. Examples include generic right-angled triangular billiards, which we cover in Chapter 6.

3. *Irrational triangular billiards:* all angles are irrational multiples of π, *i.e.* $\alpha, \beta \in \pi(\mathbb{R} \setminus \mathbb{Q})$. We will further subdivide this category in Section 1.4.

1.2 Ergodicity and mixing

Now that we defined triangular billiards, we shall review the dynamical properties we are interested in investigating. We provide a gentle introduction, focusing on the necessary

information for this thesis, following mainly [14] and [52].

Definition 1.2. Let X be a set. A σ-algebra $\mathfrak{F}$ on X is a nonempty collection of subsets of X with two properties:

(i) it is closed under countable unions; *i.e.* if $A_i \in \mathfrak{F}$ for all $i \geq 1$, then $\cup_{i=1}^{\infty} A_i \in \mathfrak{F}$

(ii) it is closed under taking complements, *i.e.* if $A \in \mathfrak{F}$, then $A^c = X \setminus A \in \mathfrak{F}$.

A pair $(X, \mathfrak{F})$ is called a measurable space and the sets $A \in \mathfrak{F}$ are said to be measurable.

Definition 1.3. A measure μ on $(X, \mathfrak{F})$ is a function $\mu : \mathfrak{F} \to \mathbb{R} \cup \{+\infty\}$ with the following properties:

(i) it is nonnegative, *i.e.* $\mu(A) \geq 0$ for all $A \in \mathfrak{F}$;

(ii) the empty set has zero measure, *i.e.* $\mu(\emptyset) = 0$;

(iii) μ is σ-additive (or countably additive), *i.e.* if $\{A_i\}_{i=1}^{\infty} \in \mathfrak{F}$ and $A_i \cap A_j = \emptyset$ for $i \neq j$, then $\mu(\cup_{i=1}^{\infty} A_i) = \sum_{i=1}^{\infty} \mu(A_i)$.

We say that μ is a probability measure if $\mu(X) = 1$ and call $(X, \mathfrak{F}, \mu)$ a probability space.

Remark. We only consider probability measures.

Definition 1.4. Let $(X, \mathfrak{F})$ be a measurable space. A transformation $T : X \to X$ is said to be measurable if $T^{-1}(B) \in \mathfrak{F}$ for every $B \in \mathfrak{F}$.

Definition 1.5. Let $\mathsf{M}(X)$ denote the set of all probability measures on $(X, \mathfrak{F})$. A measurable transformation $T : X \to X$ induces a map $T_* : \mathsf{M}(X) \to \mathsf{M}(X)$ defined by $(T_*\mu)(B) = \mu(T^{-1}B)$ for every $\mu \in \mathsf{M}(X)$ and $B \in \mathfrak{F}$. We then say that a measure $\mu \in \mathsf{M}(X)$ is T-invariant if $T_*\mu = \mu$. We denote by $\mathsf{M}_T(X)$ the set of all T-invariant probability measures on X and refer to a quadruple $(X, \mathfrak{F}, T, \mu)$, $\mu \in \mathsf{M}_T(X)$, as a measure preserving transformation.

Definition 1.6. Let $(X, \mathfrak{F}, T, \mu)$ be a measure preserving transformation. We say a

measurable set $B \subset X$ is almost T-invariant if $\mu(T^{-1}(B)\Delta B) = 0$ and T-invariant if $T(B) = B$.

Remark. If $T(B) \subset B$ and $T(B^c) \subset B^c$, then B is T-invariant.

Definition 1.7. A T-invariant measure $\mu \in \mathsf{M}_T(X)$ is said to be ergodic if for any almost T-invariant set $B \subset X$ we have $\mu(B) = 0$ or $\mu(B) = 1$.

The following result can be found in, *e.g.* [52, Theorem 1.4]

Theorem 1.1 (Poincaré's Recurrence Theorem)**.** Let $(X, \mathfrak{F}, T, \mu)$ be a measure preserving transformation. Let $E \in \mathfrak{F}$ with $\mu(E) > 0$. Then μ-almost all points of E return infinitely often to E under iterations by T, *i.e.* there exists $F \subset E$ with $\mu(F) = \mu(E)$ such that for each $x \in F$ there is a sequence $n_1 < n_2 < n_3 < \cdots$ of natural numbers with $T^{n_i}(x) \in F$ for each i.

Using this theorem, we can define the Poincaré return map as follows.

Definition 1.8. Let $(X, \mathfrak{F}, T, \mu)$ be a measure preserving transformation and $E \in \mathfrak{F}$ with $\mu(E) > 0$. Then the map

$$T_E(x) = T^{n_E(x)}(x), \quad n_E(x) = \min\{n \geq 1 \,|\, T^n(x) \in E\}$$

is defined for μ-almost every point in E. We call T_E the Poincaré return map and E its corresponding Poincaré cross section.

Definition 1.9. Let $(X, \mathfrak{F}, T, \mu)$ be a measure preserving transformation and $f : X \to \mathbb{R}$ a measurable function. For every $x \in X$ the sequence $\{f(T^n x)\}$ of values of f on the trajectory of x can be regarded as a time series. Its partial sums

$$S_n(x) = \frac{1}{n}(f(x) + f(Tx) + \cdots + f(T^{n-1}x))$$

are called ergodic sums. The limit

$$F_+(x) = \lim_{n\to+\infty} S_n(x)\,,$$

if it exists, is called the (forward) time average (or ergodic average) of the function f along the orbit of x.

Definition 1.10. Let $(X, \mathfrak{F}, T, \mu)$ be a measure preserving transformation.

(i) T is weakly mixing if for all pairs of measurable sets $A, B \in \mathfrak{F}$

$$\lim_{n\to\infty} \frac{1}{n} \sum_{i=0}^{n-1} |\mu(T^{-i}A \cap B) - \mu(A)\mu(B)| = 0\,.$$

(ii) T is (strongly) mixing if for all pairs of measurable sets $A, B \in \mathfrak{F}$

$$\lim_{n\to+\infty} \mu(T^{-n}A \cap B) = \mu(A)\mu(B)\,,$$

Remark.

- Every (strongly) mixing transformation is weakly mixing and every weakly mixing transformation is ergodic (see *e.g.* [52, p. 40]).
- For an intuitive description of mixing, note that $x \in T^{-n}A$ is equivalent to $T^n(x) \in A$. We are speaking about events $x \in B$ (x at time 0) and $T^n(x) \in A$ (the image of x at time n). Thus mixing is commonly interpreted as asymptotic independence of the distant future from the present.
- It can be shown for an intuitive description of weak mixing is that for each set $A \in \mathfrak{F}$ the sequence $T^{-n}A$ becomes independent of any other set $B \in \mathfrak{F}$ provided we neglect a few instants of time.

We can also reformulate the mixing concepts using functions, which is useful for

specific calculations (see *e.g.* [52, Theorem 1.23]).

Theorem 1.2. Let $(X, \mathfrak{F}, T, \mu)$ be a measure preserving transformation. Let $L^2_\mu(X)$ be the Hilbert space of all μ-square integrable functions on X with the inner product given by $\langle f, g\rangle_\mu = \int_X f\bar{g}\,\mathrm{d}\mu$.

(i) The following are equivalent:

(a) T is ergodic.

(b) For all $f, g \in L^2_\mu(X)$, $\lim_{n\to\infty} \frac{1}{n}\sum_{i=0}^{n-1}\langle f\circ T^i, g\rangle_\mu = \langle f\rangle_\mu\langle g\rangle_\mu$.

(c) For all $f \in L^2_\mu(X)$, $\lim_{n\to\infty} \frac{1}{n}\sum_{i=0}^{n-1}\langle f\circ T^i, f\rangle_\mu = \langle f\rangle^2_\mu$.

(ii) The following are equivalent:

(a) T is weakly mixing.

(b) For all $f, g \in L^2_\mu(X)$, $\lim_{n\to\infty} \frac{1}{n}\sum_{i=0}^{n-1}|\langle f\circ T^i, g\rangle_\mu - \langle f\rangle_\mu\langle g\rangle_\mu| = 0$.

(c) For all $f \in L^2_\mu(X)$, $\lim_{n\to\infty} \frac{1}{n}\sum_{i=0}^{n-1}|\langle f\circ T^i, f\rangle_\mu - \langle f\rangle^2_\mu| = 0$.

(d) For all $f \in L^2_\mu(X)$, $\lim_{n\to\infty} \frac{1}{n}\sum_{i=0}^{n-1}|\langle f\circ T^i, f\rangle_\mu - \langle f\rangle^2_\mu|^2 = 0$.

(iii) The following are equivalent:

(a) T is (strongly) mixing.

(b) For all $f, g \in L^2_\mu(X)$, $\lim_{n\to\infty}\langle f\circ T^n, g\rangle_\mu = \langle f\rangle_\mu\langle g\rangle_\mu$.

(c) For all $f \in L^2_\mu(X)$, $\lim_{n\to\infty}\langle f\circ T^n, f\rangle_\mu = \langle f\rangle^2_\mu$.

Definition 1.11. Given $f, g \in L^2_\mu(X)$, the quantity

$$C_{fg}(n) = \langle f\cdot(g\circ T^n)\rangle_\mu - \langle f\rangle_\mu\langle g\rangle_\mu \tag{1.6}$$

is called the *correlation function* between observables f and g at time n. If $f \equiv g$, the

correlation function is called autocorrelation function of f and we denote it by C_f. We further define

$$\hat{C}_f(n) = \langle f \cdot (f \circ T^n) \rangle_\mu$$

and call it *non-discounted* autocorrelation function of the observable f.

Definition 1.12. A sequence $\{d_i\}_{i=0}^{\infty}$ is said to be Cèsaro convergent, if the sequence $\{\mathscr{C}_i\}_{i=0}^{\infty}$ defined as

$$\mathscr{C}_n = \frac{1}{n} \sum_{i=1}^{n} d_i$$

converges. We call $\{\mathscr{C}_i\}_{i=0}^{\infty}$ the associated Cèsaro sequence.

Remark. Using Theorem 1.2, we have the following:

- Mixing is equivalent to the convergence of correlations (or autocorrelations) to zero for all μ-square integrable observables f, g.
- Weak mixing is equivalent to the convergence of the Cèsaro sequence associated to the absolute value of the autocorrelation function to zero for all μ-square integrable observables.
- Ergodicity is equivalent to the convergence of the Cèsaro sequence associated to the autocorrelation function to zero for all μ-square integrable observables.

1.3 Explanation of different tests for ergodicity and mixing

For our purposes we have mainly investigated the momentum p and the observable $\zeta(s) = \sin(2\pi s/L)$, where L is the circumference of the triangle. We also performed several numerical simulations with different combinations of p and ζ with the conclusion that the behaviour was very similar to that of both p and ζ. The choice of momentum as the main observable stems from the fact that whereas the dynamics in the rational case usually seems to be ergodic with respect to the Lebesgue measure in the positional s coordinate, it is restrained to only a finite number of possible values in momentum.

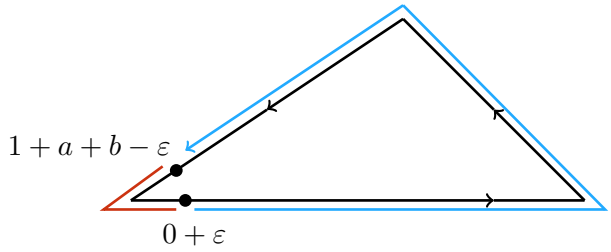

Figure 1.8: Illustration for the reason why ζ is a better observable for autocorrelation functions than just the position s. The light blue arrow indicates the distance between the two points in our coordinate system. The red line illustrates how close they really are.

Therefore, if (weakly) mixing behaviour in the momentum is observed, it is more likely to correspond to the overall behaviour. As to explain the strange observable ζ in position, one needs to look back at the geometry of the triangle. There, we see that even though points $0 + \varepsilon$ and $1 + a + (b - \varepsilon)$ are, in fact, very close together (1.3), due to the nature of the chosen coordinates they are far apart. However, if we choose ζ for our observable, this problem disappears.

1.4 Notation

As explained in Section 1.2, studying ergodic properties of triangular billiards requires calculating compositions of the map T with itself. However, one is not able to easily write down the expression for the n-th iterate T^n of the map (see Eq. (1.5)) in closed form due to the discontinuities introduced by the quantity p_s. Therefore, almost all of our findings are results of numerical simulations. Due to the nature of numerical computation, we were only able to investigate a few examples of triangular billiards. We thus had to make a careful choice for the geometries of the triangular billiards used in our simulations.

For simulations of irrational triangular billiards, our choice for the angles is as follows:

- GM $= \pi\frac{\sqrt{5}-1}{4}$, an angle constructed from the golden mean
- SM $= \pi\frac{\sqrt{2}-1}{4}$, an angle constructed from the silver mean
- SQ2 $= \pi\frac{\sqrt{2}}{4}$

	α	α/π
SM	0.325	0.104
Log3	0.749	0.239
GM	0.971	0.309
SQ2	1.111	0.354
PiPi	1.234	0.393
SQ3	1.360	0.433

Table 1-B: Table summarising the values of angles considered throughout this thesis. We include the value of the angle, denoted by α, and the value of the angle expressed as a multiple of π, denoted by α/π. All values are rounded to 3 decimal places.

- SQ3 $= \pi\frac{\sqrt{3}}{4}$
- Log3 $= \pi\frac{\log_{10} 3}{4}$
- PiPi $= \frac{\pi^2}{8}$

Actual values of these angles, ordered by their size, can be found in Table 1-B.

Part II demonstrates that neither the actual value nor the number theoretical properties of the angles qualitatively influence the overall dynamical behaviour. However, the shape of the triangular billiard plays a greater, qualitative, role in the dynamical behaviour. To avoid confusion, we use the following terminology for triangular billiards:

- asymmetric: all angles are different; the usual generic triangular billiards. Actual triangular billiards we considered can be found in Figure 1.9. Chapter 4 is dedicated to their dynamical behaviour.
- slightly asymmetric: triangular billiards where two angles differ by a small ε
- symmetric: isosceles triangular billiards with $\alpha = \beta$. We adopted this name to make talking about *slightly asymmetric* and *symmetric* triangular billiards easier. Symmetric triangular billiards for which simulations were performed are plotted in Figure 1.10. Symmetric and slightly asymmetric triangular billiards are further studied in Chapter 5.
- right-angled: triangular billiards where one angle, usually β, is $\frac{\pi}{2}$. A special case

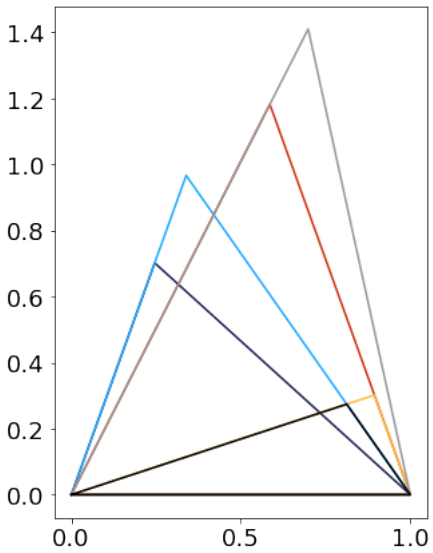

Figure 1.9: Asymmetric triangular billiards from Chapter 4: SM-GM (black), SM-PiPi (yellow), PiPi-GM (light blue), SQ2-PiPi (red), PiPi-Log3 (dark blue), SQ2-SQ3 (grey).

of asymmetric triangular billiards. Some of the right-angled triangular billiards we simulated are in Figure 1.10. Results about right-angled triangular billiards can be found in Chapter 6.

- thin: triangular billiards where at least one angle is $\lesssim 0.15$. We arrive at this value by studying the behaviour of phase portraits, see Chapter 7.

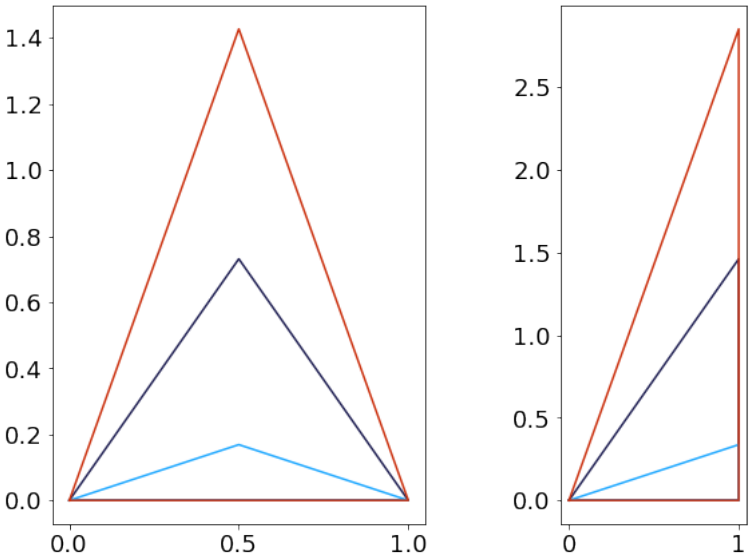

Figure 1.10: Left: Symmetric triangular billiards studied in Chapter 5; PiPi-PiPi (red), GM-GM (dark blue), SM-SM (light blue).
Right: Right-angled triangular billiards presented in Chapter 6; PiPi-Pi2 (red), GM-Pi2 (dark blue), SM-Pi2 (light blue).
Note that while the x and y scales are the same within the figures, they differ between the two figures.

Chapter 2

Algorithms

A rigorous study of dynamical properties of triangular billiards is difficult due to problems outlined in the previous chapter. As a result, most of this thesis is based on numerical simulations which were coded from scratch. We decided to include this chapter to thoroughly document algorithms used, something often omitted in the literature. The code can be found at `https://github.com/katz313/Triangular-Billiards`.

This chapter is organised as follows: the structure of the main code, along with an outline of its development, is in Section 2.1. Section 2.2 includes the overview of the tests for mixing. The details about the different tests for ergodicity are in Section 2.3.

2.1 Code and its optimization

As mentioned above, the code used to investigate dynamical properties of various triangular billiards has been coded from scratch. We used Python, for its convenience and prevalence in the scientific community. All computations were done in double precision.

The core of the simulation is a function computing the coordinates of the next collision with the boundary. The natural way how to do this is using the billiard map and Birkhoff coordinates (s, p).

Due to the nature of our investigation, the core functions simulating the collisions needed to be coded as efficiently as possible. I would like to acknowledge the help of Julia Slipantschuk with rewriting the `next_collision` and `N_collisions` functions into Cython, along with elegantly coding the map, Eq. (1.5), into objects.

Algorithm 1: `next_collision`$(s_0, p_0, \alpha, \beta)$

compute s, p using the map from Eq. (1.5);
return s, p

Algorithm 2: `N_collisions`$(s_0, p_0, \alpha, \beta, N)$

s, p = zero vectors of dimension N;
$s[0] = s_0$;
$p[0] = p_0$;
for $0 \leq i \leq N-1$ **do**
  $s[i+1], p[i+1] =$ `next_collision`$(s[i], p_[i], \alpha, \beta)$;
return s, p

As explained in Chapter 1, some of the tests we used involve computing the autocorrelation function. To do that, we use a standard Fast Fourier Transform (FFT) approach. Python has several libraries with efficient FFT algorithms. However, as we average over large ensembles, it was not possible to run it on a normal desktop computer in order to get the desired time scales. Therefore, we used Queen Mary's Hight Performance Computing facility Apocrita to run the simulations. Thanks to a collaboration with the Research Software Engineering team in ITS Research, we were able to further optimize the FFT computation. They helped us implement the Fastest Fourier Transform in the West (FFTW) library in our code, which enables saving a so-called *wisdom*. *Wisdom* is a file containing saved information about how to optimally compute Fourier transform of various sizes ([28]). As we are computing thousand(s) of FFTs of vectors in one autocorrelation calculation, see details below, this helped us to speed up the computation and thus increase the length of the considered orbits. The most computationally expensive calculations were done to compute the autocorrelation functions, requiring about 50GB of RAM and 3 days.

2.2 Tests for mixing

We will start our algorithm overview with tests for mixing, as some of these algorithms will be used to test for ergodicity as well. To determine whether an ergodic system is, in fact, (weakly) mixing, one needs to look at its autocorrelation functions as discussed in Section 1.2. However, in our numerical experiments, we discovered that in the interesting cases, the method of computation of the autocorrelation function is a key factor in the resulting behaviour.

Computing autocorrelation functions

Firstly, we present the different methods of computing the autocorrelation functions, as they are used in some of the other tests. We use two different methods of computing the autocorrelation functions, the `cuts` and `rand` methods. These two methods differ in how we treat the ensemble average.

In the case of the `cuts` method (`corr_cuts`, Alg. 3), we compute one long orbit of length $M \cdot N$ and cut it into shorter pieces of length N. We use the FFT subroutine `fft_aux` (see Alg. 5) and Wiener-Khinchin theorem (see Section 2.2.1) to compute the autocorrelation. The final step is to take the ensemble average over all the pieces.

Algorithm 3: `corr_cuts`(α, β, s_0, p_0, N, M, `discount`, f)

corr = zero vector of dimension N;
for $0 \leq i < M$ **do**
    s, p = `N_collisions`(s_0, p_0, α, β, N);
    $s_0 = s[-1]$;
    $p_0 = p[-1]$;
    v = chosen observable f computed from s and p;
    corr += `fft_aux`(v, `discount`);
corr = corr/M;
return corr

For the `rand` method (`corr_rand`, Alg. 4), we generate M uniformly distributed initial conditions and compute an orbit of length N for each of them. We then use the FFT subroutine `fft_aux` and Wiener-Khinchin theorem to compute the individual autocorrelations. Finally, we take the ensemble average over all the initial conditions.

Algorithm 4: `corr_rand`(α, β, N, M, `discount`, f)

$S = \mathcal{U}_{(0,L)}(M)$;

$P = \mathcal{U}_{(-1,1)}(M)$;

corr = zero vector of dimension N;

for $0 \leq i < M$ **do**

  $s, p =$ `N_collisions`($S[i]$, $P[i]$, α, β, N);

  $v =$ chosen observable f computed from s and p;

  corr += `fft_aux`(v, `discount`);

corr = corr$/M$;

return corr

Moreover, we also look at discounted and non-discounted autocorrelation functions. The distinction is done using an argument `discount`. If `discount = True`, then we, effectively, subtract the term $\langle f \rangle_\mu^2$ in Eq. (1.6). We call this autocorrelation *discounted*. If, on the other hand, `discount = False`, then we do not subtract $\langle f \rangle_\mu^2$ and, in the end, we compute

$$\hat{C}_f(n) = \langle f \cdot (f \circ T^n) \rangle_\mu \,, \tag{2.1}$$

and, in line with Definition 1.11, call it *non-discounted* autocorrelation function of observable f.

For the numerical computation of individual autocorrelation functions, we use the standard FFT approach (see Algorithm 5).

Algorithm 5: `fft_aux`(v, `discount`)

$\hat{v}$ = FFT of vector v;

$\hat{v} = \hat{v}\,\overline{\hat{v}}/\texttt{len}(\hat{v})$, where $\texttt{len}(\hat{v})$ denotes the length of vector $\hat{v}$;

if *discount* **then**

  $\hat{v}[0] = 0$;

$\hat{v}$ = inverse FFT of $\hat{v}$;

$\hat{v} = \hat{v}/\hat{v}[0]$ to normalise it;

return $\hat{v}$;

2.2.1 Wiener–Khinchin Theorem for the discrete Fourier transform

We include this subsection to demonstrate that the result of Algorithms 3 and 4 actually produce the desired autocorrelation function. We start by recalling some facts about the discrete Fourier transform.

Let us fix $N \in \mathbb{N}$. Given $x \in \mathbb{C}^N$ its discrete Fourier transform $\mathcal{F}_N(x) \in \mathbb{C}^N$ is given by the *analysis formula*

$$\mathcal{F}_N(x)_m \equiv \hat{x}_m = \frac{1}{N_+} \sum_{j=0}^{N-1} x_j \exp\left\{-\frac{2\pi i}{N} jm\right\}$$

for all $m \in \{0, \cdots, N-1\}$. The original vector x can be recovered from its discrete Fourier transform $\hat{x}$ by the *synthesis formula*

$$x_n = \mathcal{F}_N^{-1}(\hat{x})_n = \frac{1}{N_-} \sum_{j=0}^{N-1} \hat{x}_j \exp\left\{\frac{2\pi i}{N} jn\right\}$$

for all $n \in \{0, \cdots, N-1\}$ provided that the normalisation N_+ and N_- are chosen such that

$$N_+ N_- = N\,.$$

Taking $N_+ = 1$ and $N_- = N$ appears to be a popular choice, but we shall keep the discussion general in the following as not all implementations seem to follow this

convention. In the following we shall drop the subscript N for $\mathcal{F}$ and $\mathcal{F}^{-1}$ if the ambient dimension is understood.

Note that for a given $\hat{x}$, the RHS of the synthesis formula makes sense not just for $n \in \{0, \ldots, N-1\}$, but for any $n \in \mathbb{Z}$ in which case we have the *extended* or *circular synthesis formula*

$$\frac{1}{N_-} \sum_{k=0}^{N-1} \hat{x}_k \exp\left\{-\frac{2\pi i}{N} kn\right\} = x_{n \bmod N} \quad (\forall n \in \mathbb{Z}),$$

since, for any $r \in \mathbb{Z}$ and any $l \in \{0, \ldots, N-1\}$, we have

$$\frac{1}{N_-} \sum_{k=0}^{N-1} \hat{x}_k \exp\left\{-\frac{2\pi i}{N} k(l+rN)\right\} = \frac{1}{N_-} \sum_{k=0}^{N-1} \hat{x}_k \exp\left\{-\frac{2\pi i}{N} kl\right\}.$$

We shall derive a Wiener–Khinchin type theorem in the current set-up. Suppose we are given $x, y \in \mathbb{C}^N$ with corresponding discrete Fourier transforms $\hat{x}, \hat{y} \in \mathbb{C}^N$. Firstly, we derive the so-called *circular cross-correlation formula*

$$\mathcal{F}^{-1}(\bar{\hat{x}} \cdot \hat{y})_n = \frac{1}{N_+} \sum_{m=0}^{N-1} \bar{x}_m y_{(m+n) \bmod N}.$$

In order to see this, note that

$$\begin{aligned}
\mathcal{F}^{-1}(\bar{\hat{x}} \cdot \hat{y})_n &= \frac{1}{N_-} \sum_{k=0}^{N-1} \bar{\hat{x}}_k \hat{y}_k \exp\left\{\frac{2\pi i}{N} kn\right\} \\
&= \frac{1}{N_-} \sum_{k=0}^{N-1} \frac{1}{N_+} \sum_{m=0}^{N-1} \bar{x}_m \hat{y_k} \exp\left\{\frac{2\pi i}{N} k(m+n)\right\} \\
&= \frac{1}{N_+} \sum_{m=0}^{N-1} \bar{x}_m \frac{1}{N_-} \sum_{k=0}^{N-1} \hat{y_k} \exp\left\{\frac{2\pi i}{N} k(m+n)\right\} \\
&= \frac{1}{N_+} \sum_{m=0}^{N-1} \bar{x}_m y_{(m+n) \bmod N},
\end{aligned}$$

where we first used the definition of $\hat{x}$, then exchanged the two sums, and finally used the extended synthesis formula for y. In particular, we obtain the following Wiener–Khinchin

type formula

$$\mathcal{F}^{-1}(|\hat{x}|^2)_n = \frac{1}{N_+}\sum_{m=0}^{N-1} \bar{x}_m x_{(m+n) \bmod N}\,, \tag{2.2}$$

which provides an effective way of calculating autocorrelation functions of discrete signals.

We can also obtain a 'zero-discounted' version of the Wiener–Khinchin formula (which is the inverse discrete Fourier transform of the modulus squared of the discrete Fourier transform of x, for which the zero entry of $|\hat{x}|^2$ has been set to 0) by letting

$$\hat{y}_k = \begin{cases} \hat{x}_k & k > 0 \\ 0 & k = 0 \end{cases}$$

in the cross-correlation formula, which gives

$$\begin{aligned}
\mathcal{F}^{-1}(\bar{\hat{x}} \cdot \hat{y})_n &= \frac{1}{N_-}\sum_{k=0}^{N-1} \bar{\hat{x}}_k \hat{y}_k \exp\left(\frac{2\pi i}{N} kn\right) \\
&= \frac{1}{N_-}\sum_{k=1}^{N-1} \bar{\hat{x}}_k \hat{x}_k \exp\left(\frac{2\pi i}{N} kn\right) \\
&= \frac{1}{N_-}\left(\sum_{k=0}^{N-1} \bar{\hat{x}}_k \hat{x}_k \exp\left(\frac{2\pi i}{N} kn\right) - \bar{\hat{x}}_0 \hat{x}_0\right) \\
&= \frac{1}{N_+}\sum_{m=0}^{N-1} \bar{x}_m x_{(m+n) \bmod N} - \frac{1}{N_-}\frac{1}{N_+^2}\left|\sum_{k=0}^{N-1} x_k\right|^2 \\
&= \frac{1}{N_+}\sum_{m=0}^{N-1} \bar{x}_m x_{(m+n) \bmod N} - N_-\left|\frac{1}{N}\sum_{k=0}^{N-1} x_k\right|^2 .
\end{aligned}$$

From now on, we shall assume that $N_+ = 1$ and $N_- = N$, as implemented in the packages we used. Then the zero-discounted version gives for $x \in \mathbb{R}^N$

$$\frac{1}{N}\mathcal{F}^{-1}(\bar{\hat{x}} \cdot \hat{y})_n = \frac{1}{N}\sum_{m=0}^{N-1} x_m x_{(m+n) \bmod N} - \left(\frac{1}{N}\sum_{k=0}^{N-1} x_k\right)^2 .$$

If x_m is obtained as a time series $x_m = f(T^m\xi)$ of an ergodic transformation T with

invariant measure μ and a real-valued observable f then, by the ergodic theorem,

$$\frac{1}{N}\sum_{m=0}^{N-1} x_m x_{m+n} - \left(\frac{1}{N}\sum_{k=0}^{N-1} x_k\right)^2 \xrightarrow{N\to\infty} \int f \cdot f\circ T^n \, d\mu - \left(\int f \, \mathrm{d}\mu\right)^2 \text{ for } \mu\text{-a.e. } \xi\,,$$

which is the above, except for the mod N term. In order to examine the convergence in more detail we introduce the following methods, taking as input a real-valued sequence $x \in \mathbb{R}^{\mathbb{N}_0}$:

The *basic method* with parameters $N \in \mathbb{N}$ and $n \in \mathbb{N}_0$, $n < N$:

$$\mathcal{M}_N(x)_n = \frac{1}{N}\sum_{m=0}^{N-1} x_m x_{(m+n) \bmod N}\,. \tag{2.3}$$

The *basic discounted method* with parameters $N \in \mathbb{N}$ and $n \in \mathbb{N}_0$, $n < N$:

$$\mathcal{M}^0_N(x)_n = \frac{1}{N}\sum_{m=0}^{N-1} x_m x_{(m+n) \bmod N} - \left(\frac{1}{N}\sum_{k=0}^{N-1} x_k\right)^2 .$$

For comparison, we also introduce the following functions on $x \in \mathbb{R}^{\mathbb{N}_0}$, with parameters $N \in \mathbb{N}$ and $n \in \mathbb{N}_0$, $n < N$:

$$\mathcal{C}_N(x)_n = \frac{1}{N}\sum_{m=0}^{N-1} x_m x_{m+n}\,,$$

$$\mathcal{C}^0_N(x)_n = \frac{1}{N}\sum_{m=0}^{N-1} x_m x_{m+n} - \left(\frac{1}{N}\sum_{k=0}^{N-1} x_k\right)^2 .$$

We have the following basic error estimate

$$|\mathcal{C}_N(x)_n - \mathcal{M}_N(x)_n| = \left|\mathcal{C}^0_N(x)_n - \mathcal{M}^0_N(x)_n\right| = \left|\frac{1}{N}\sum_{m=N-n}^{N-1} x_m(x_{m+n} - x_{m+n-N})\right| \le 2\frac{n}{N}\|x\|^2_\infty\,.$$

The above implies that, for x a time-series obtained from an ergodic transformation

$x_m = f(T^m\xi)$ as before, that, for fixed $n \in \mathbb{N}_0$,

$$\mathcal{M}_N(x)_n \xrightarrow{N\to\infty} \int f \cdot f \circ T^n \,\mathrm{d}\mu \quad \text{for } \mu\text{-a.e. } \xi$$

and

$$\mathcal{M}^0_N(x)_n \xrightarrow{N\to\infty} \int f \cdot f \circ T^n \,\mathrm{d}\mu - \left(\int f \,\mathrm{d}\mu\right)^2 \text{ for } \mu\text{-a.e. } \xi$$

As the speed of convergence in the ergodic theorem is a very delicate issue not much more than the above can be said.

Let us have a look at the cuts method (see Alg. 3), which relies on taking a vector x of length MN and chopping it into M vectors $x^{(k)}$, $k = 1, \ldots, M$ of length N by defining $x^{(k)}_m = x_{(k-1)N+m}$ and then averaging over any of the two basic methods yielding:

The cuts method with parameters $M, N \in \mathbb{N}$ and $n \in \mathbb{N}_0$, $n < N$:

$$\mathcal{M}_{M,N}(x)_n = \frac{1}{M}\sum_{k=1}^{M} \mathcal{M}_N(x^{(k)})_n \,,$$

and the discounted cuts method with parameters $M, N \in \mathbb{N}$ and $n \in \mathbb{N}_0$, $n < N$:

$$\mathcal{M}^0_{M,N}(x)_n = \frac{1}{M}\sum_{k=1}^{M} \mathcal{M}^0_N(x^{(k)})_n \,.$$

Using the basic error estimate above, we obtain

$$|\mathcal{C}_{MN}(x)_n - \mathcal{M}_{M,N}(x)_n| = \left|\mathcal{C}^0_{MN}(x)_n - \mathcal{M}^0_{M,N}(x)_n\right| \leq 2\frac{n}{N}\|x\|^2_\infty \,.$$

Note that these error estimates hold for $n < N$. In our calculations, we only consider the first 0.1% of the computed vector, therefore, this condition holds.

Therefore we conclude that for x a time-series obtained from an ergodic transforma-

tion $x_m = f(T^m\xi)$, for fixed $n \in \mathbb{N}_0$ and $M \in \mathbb{N}$,

$$\mathcal{M}_{M,N}(x)_n \xrightarrow{N\to\infty} \int f \cdot f \circ T^n \,\mathrm{d}\mu \text{ for } \mu\text{-a.e. } \xi$$

and

$$\mathcal{M}^0_{M,N}(x)_n \xrightarrow{N\to\infty} \int f \cdot f \circ T^n \,\mathrm{d}\mu - \left(\int f \,\mathrm{d}\mu\right)^2 \text{ for } \mu\text{-a.e. } \xi\,.$$

Hence the cuts and discounted cuts methods produce the desired result.

Finally, we discuss the rand method, which is best understood in terms of Monte Carlo integration. Therefore, we start with briefly reviewing the basics of it.

Let $(X, \mathfrak{F}, \mu)$ be a probability space and $Y : X \to X$ be a random variable such that $\mathbb{P}(Y \in F) = \mu(F)$ for any $F \in \mathfrak{F}$. Suppose that $\phi : X \to \mathbb{C}$ is μ-integrable. Then an approximation of the integral $\int_X \phi \,\mathrm{d}\mu$ can be obtained as follows. Let $(Y_k)_{k\in\mathbb{N}}$ be a sequence of random variables $Y_k : X \to X$, each with law μ. For every $M \in \mathbb{N}$ we can form the average

$$\frac{1}{M}\sum_{k=1}^{M} \phi\left(Y_k\right). \tag{2.4}$$

Now, since the random variables Y_k are independent, so are the random variables $\phi(Y_k)$. Moreover, as ϕ is μ-integrable, we have

$$\mathbb{E}(|\phi(Y_k)|) = \int_X |\phi| \,\mathrm{d}\mu < \infty$$

for all $k \in \mathbb{N}$. Since the first moments are finite, the strong law of large numbers implies ([34, Thm. 5.17]) that we almost surely have

$$\frac{1}{M}\sum_{k=1}^{M} \phi\left(Y_k\right) \xrightarrow{M\to\infty} \mathbb{E}(\phi(Y_1)) = \int_X \phi \,\mathrm{d}\mu\,.$$

Hence we are able to obtain almost surely convergent approximations of the integral $\int_X \phi \,\mathrm{d}\mu$ by sampling independently from X following the law μ and calculating the empirical means from Eq. (2.4). In our case, X is a rectangle $R = [0, L] \times [-1, 1] \in \mathbb{R}^2$

and μ is obtained from 2-dimensional Lebesgue measure Leb as

$$\mu(F) = \frac{\mathrm{Leb}(F)}{\mathrm{Leb}(R)} = \frac{1}{2L}\mathrm{Leb}(F)$$

for every Lebesgue measurable F, *i.e.* we are sampling uniformly at random in the rectangle R.

We now return to the rand method. It uses the *basic* method, see Eq. (2.3), applied to $x_n = f(T^n\xi)$ followed by randomly sampling over ξ. More precisely, fix $N \in \mathbb{N}$ and $n \in \mathbb{N}_0$, with $n < N$ and consider the function $\phi_{N,n} : X \to \mathbb{R}$ given by

$$\phi_{N,n}(\xi) = \frac{1}{N}\sum_{m=0}^{N-1} f(T^m\xi)f(T^{(m+n) \bmod N}\xi)\,.$$

For $Y : X \to X$ a random variable with law μ we have

$$\begin{aligned}
\mathbb{E}(|\phi_{N,n}(Y)|) &\le \frac{1}{N}\sum_{m=0}^{N-1}\int_X |f|\circ T^m \cdot |f|\circ T^{(m+n) \bmod N}\mathrm{d}\mu \\
&= \frac{1}{N}\left(\sum_{m=0}^{N-1-n}\int_X |f|\circ T^m \cdot |f|\circ T^{m+n}\mathrm{d}\mu \right. \\
&\qquad \left. + \sum_{m=N-n}^{N-1}\int_X |f|\circ T^m \cdot |f|\circ T^{m+n-N}\mathrm{d}\mu\right) \\
&= \frac{1}{N}\left(\sum_{m=0}^{N-1-n}\int_X |f|\cdot|f|\circ T^n\mathrm{d}\mu + \sum_{m=N-n}^{N-1}\int_X |f|\cdot|f|\circ T^{N-n}\mathrm{d}\mu\right) \\
&= \frac{N-n}{N}\int_X |f|\cdot|f|\circ T^n\mathrm{d}\mu + \frac{n}{N}\int_X |f|\cdot|f|\circ T^{N-n}\mathrm{d}\mu \\
&\le \int_X |f|^2\mathrm{d}\mu = \|f\|^2_{L^2_\mu(X)}\,,
\end{aligned}$$

where we used T-invariance of the measure μ and Cauchy-Schwarz inequality in the last step. Therefore,

$$\mathbb{E}(|\phi_{N,n}(Y)|) < \infty$$

provided that $f \in L^2_\mu(X)$.

Similarly,

$$\begin{aligned}\mathbb{E}(\phi_{N,n}(Y)) &= \frac{N-n}{N}\int_X f\cdot f\circ T^n \mathrm{d}\mu + \frac{n}{N}\int_X f\cdot f\circ T^{N-n}\mathrm{d}\mu \\ &= \int_X f\cdot f\circ T^n \mathrm{d}\mu + \frac{n}{N}\int_X f\cdot (f\circ T^{N-n} - f\circ T^n)\mathrm{d}\mu\,.\end{aligned}$$

For the rand method, we sample uniformly from X following the law μ, forming the empirical means $\frac{1}{M}\sum_{k=1}^{M}\phi_N(Y_k)$, which, using the results above, converge almost surely to the expected values $\mathbb{E}(\phi_N(Y_k))$, *i.e.*

$$\frac{1}{M}\sum_{k=1}^{M}\phi_{N,n}(Y_k) \xrightarrow{M\to\infty} \mathbb{E}(\phi_{N,n}(Y)) = \int_X f\cdot f\circ T^n\mathrm{d}\mu + \frac{n}{N}\int_X f\cdot(f\circ T^{N-n} - f\circ T^n)\mathrm{d}\mu\,,$$

which gives us the correlation integral $\int_X f\cdot f\circ T^n\mathrm{d}\mu$ with an error term bounded by

$$\left|\frac{n}{N}\int_X f\cdot(f\circ T^{N-n} - f\circ T^n)\mathrm{d}\mu\right| \leq \frac{2n}{N}\|f\|^2_{L^2_\mu(X)}$$

that consequently tends to zero as $N\to\infty$. In our calculations, we usually use $N = 2^{30}\sim 10^9$ and $M = 10^3$.

2.3 Tests for ergodicity

In this section, we present algorithmic implementations of tests discussed in Chapter 5.

Order parameter

When investigating ergodicity of Lebesgue measure in symmetric triangular billiards, we introduce an order parameter Φ_f for the observable f as follows

$$\Phi_f(N) = \frac{1}{N}\sum_{n=0}^{N-1}\langle f\cdot f\circ T^n\rangle_{\text{Leb.}}\,,$$

as the necessary condition of the ergodicity of the invariant measure μ is the convergence of the Cèsaro sequence associated to the non-discounted autocorrelation function to zero

for all μ-square integrable observables with $\langle f \rangle_{\text{Leb.}} = 0$, see Section 1.2 and Section 5.4 for motivation and more details. For computations, we use the `rand` method. Algorithm 6 gives the algorithmic overview.

Algorithm 6: `phi_f`(N, M, α, β, f)

```
phi_f = zero vector of N;
running_sum = 0;
temp = corr_rand(α, β, N, M, discount = False, f) ;
for 0 ≤ i < N do
    running_sum += temp[i];
    phi_f[i] = running_sum / (i+1);
return phi_f;
```

Distribution of ergodic averages

Another test, introduced in Chapter 5 studies the distribution of ergodic averages of momentum. To this end, we first generate M uniformly distributed initial conditions. Then, we compute an orbit of length N starting from each one. We average the momenta along individual orbits, saving the means. This is done in function `pk_sum`, see Alg. 7. Once we have the vector of means, we can plot it as a histogram or use it otherwise.

Algorithm 7: `pk_sum`(N, M, α, β)

```
S = U_(0,L)(M);
P = U_(−1,1)(M);
pk = zero vector of dimension M;
for 0 ≤ i < M do
    s,p = N_collisions(S[i], P[i], α, β, N);
    pk[i] = mean(p);
return pk
```

Convergence of ergodic averages

Finally, we present the algorithm used to compute the convergence of ergodic averages, see Section 5.6 for more details. Here, in order to save space, we are saving the data logarithmically instead of saving all the values. Note that due to that, we are also returning (and saving) the number of averaged collisions (in the vector ind) so that we can correctly plot the data. The HPC version of this computation is slightly different due to the time limit for computations there — we added an intermittent saving to it and let it run for as long as possible.

Algorithm 8: `s_sum`(s, p, α, β, N)

```
running_sum = p;
counter = 0.999999;
s_sum = zero vector of dimension N;
ind = zero vector of dimension N;
iteration = 0;
j = 0;
while s_sum[-1] = 0 do
    s, p = next_collision(s, p, α, β);
    running_sum += p;
    iteration += 1;
    if i > counter then
        s_sum [j] = running_sum / (iteration+1);
        ind[j] = iteration;
        j += 1;
        counter *= 1.001
return s_sum, iteration
```

Part I

Rational triangular billiards

Chapter 3

Rational case

In this chapter, we shall discuss rational triangular billiards, *i.e.* triangular billiards with $\alpha, \beta \in \pi\mathbb{Q}$. Recall from the Introduction that there are many results in the literature about both rational triangular and polygonal billiards as the number of scattering angles occurring along any single orbit is finite, which leads to a foliation of the phase space into a collection of invariant lines. Moreover, the dynamics on these invariant lines is described by one-dimensional piecewise linear invertible maps, known as interval exchange transformations, which are also studied in other areas of mathematics, see *e.g.* [30, 49]. Our aim is to present some explicit examples of rational billiards, along with results of approximations of irrational billiards, in particular, we present results about ergodic properties of approximations for triangular billiards we study in later chapters.

The organisation of this chapter is as follows. Section 3.1 explains the phase space dynamics of rational triangular billiards. Sections 3.2 showcase a particular example of a rational triangular billiard in more detail. Lastly, Section 3.3 focuses on rational approximations of irrational triangular billiards.

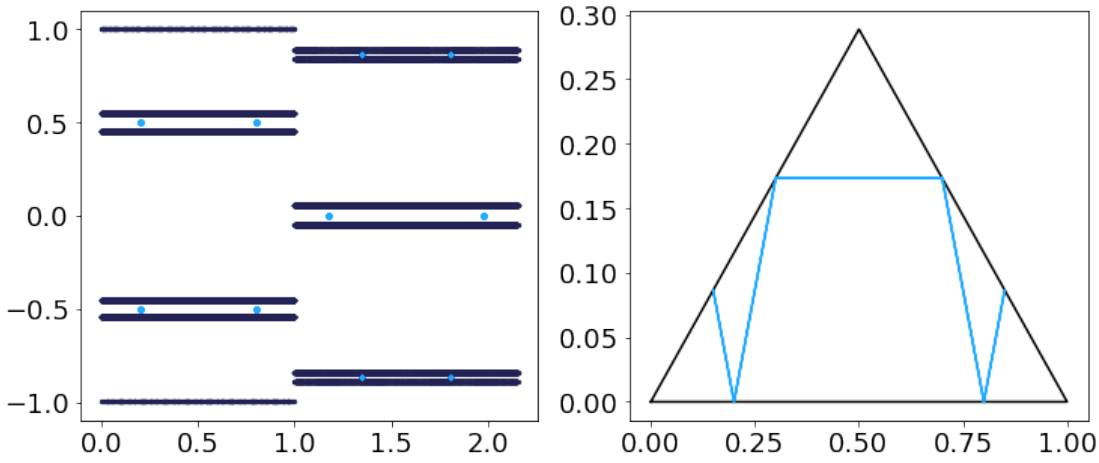

Figure 3.1: An example of a phase portrait for two particular orbits of a rational triangular billiard for $\alpha = \pi/6$, $\beta = \pi/6$ for two different initial conditions, denoted by dark blue and light blue dots. The light blue dots corresponds to the periodic orbit plotted on the right panel.

3.1 Phase space

Consider a triangular billiard with inner angles $\alpha, \beta, \gamma \in \pi\mathbb{Q}$. We can express them as $\pi\, l_i/D$, $i \in \{\alpha, \beta, \gamma\}$, with D denoting the smallest common denominator. As described in Chapter 1, we usually work in Birkhoff coordinates (s, p), with s being the position on the boundary and $p = \cos\varphi$ the tangential velocity component. The map $T(s, p) = (s', p')$ is given in Eq. (1.5). Another way to express the direction of the particle would be to look at the angle φ between the oriented boundary and the outward direction (see Figure 1.4 for details.). Then, we have $\varphi' = \pi - \lambda - \varphi$ or $\varphi' = \varphi - \lambda$ depending on whether the particle bounces to the right or left, with λ being the inner angle of the sides involved. Denoting the initial angle by φ_0, the only possible potential scattering angles for that orbit are given by the $2D$ values $\varphi_0 + \pi\, i/D$ and $-\varphi_0 + \pi\, i/D$, where $i \in \mathbb{Z}$ such that the values are contained in the domain $[0, \pi]$. Note that not all possible angles have to be visited. An example is shown in Figure 3.1.

Even if we consider an initial angle from an interval $[\varphi_0, \varphi_0 + \varepsilon]$, $\varepsilon > 0$, the resulting possible scattering angles, given by $2D$ rectangles in the phase space, do not fill in the phase space provided that ε is small enough. Lebesgue measure, therefore, cannot

be ergodic as we can construct an invariant subset with measure greater than zero. The dynamics has non-trivial constants of motion and is therefore sometimes called pseudointegrable [40]. Due to this confinement, we can reduce the dynamics to one-dimensional piecewise linear invertible maps called interval exchange transformations, see *e.g.* [30, 49]. The study of these one-dimensional simplifications of the original map reveals many interesting details of the dynamical system. We demonstrate this using a particular example.

3.2 The almost integrable case

Consider a symmetric triangular billiard with inner angles $\pi/6$, $\pi/6$ and $2\pi/3$. We will call it the Pi6-Pi6 triangular billiard for short. Note that we can obtain this triangular billiard from the integrable triangular billiard with angles $\pi/6$, $\pi/2$ and $\pi/3$ by unfolding (see last part of Section 1.1 for more details). We can further consider the unfolding of this triangular billiard. This way, we can focus on studying a geodesic flow on a flat surface instead of orbits bouncing within the triangular billiard. Unlike the few integrable cases, the flat surface resulting from the Pi6-Pi6 triangular billiard has singularities induced by the corner point corresponding to the inner angle $2\pi/6$.

The unfolding can be found in Figure 3.2. The same topological object, even though in a slightly different context, has been described in the literature, see *e.g.* [18, 40, 43]. The flat surface consists of two tori connected via a branch cut, with the two singularities caused by the obtuse angle. The branch cut is a result of the unfolding of the triangle for the case where the orientations of the corresponding sides do not match. Note that these branch cuts do not occur for the unfolding of the $\pi/6, \pi/2, \pi/3$ billiard, see Figure 1.7, which is connected to the Pi6-Pi6 triangular billiard by unfolding. The torus appears due to the fact that we identify opposite sides within each surface. Note that the topology of the surface does not depend on the way the unfolding was performed.

The unfolding in Figure 3.2 clearly shows that there are only a finite number of

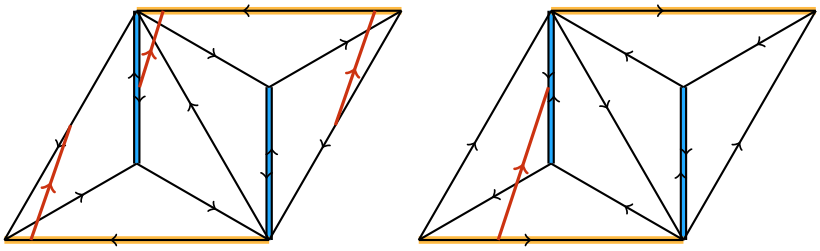

Figure 3.2: Unfolding of the almost integrable Pi6-Pi6 triangular billiard. The flat surface consists of two sheets of a torus, connected via a branch cut (light blue). An orbit (red), originating from the right sheet, has been plotted for two iterates of the Poincaré map corresponding to the Poincaré cross-section (yellow).

scattering angles for a given orbit.

3.3 Rational approximations of irrational triangular billiards

In the remainder of the thesis, we numerically simulate irrational billiards. However, as we are using standard double precision in Python, it is not entirely clear whether our simulations faithfully represent the dynamics in actual irrational triangular billiards. We therefore include this section in order to justify our numerical results. While our results are not obtained using infinite precision or by using precise formulas, we demonstrate that when we round the angles down to four decimal places, the results of our simulations stay in accordance with our expectations.

In order to show that results presented in the following chapters are valid, we consider our 'default' two triangular billiards SM-GM and GM-GM, while rounding their angles to different numbers of decimal places. Let us illustrate this on an example. The angle we denote as GM is given by $\pi(\sqrt{5}-1)/4$. In our calculation, we construct rounded angles from GM as $\pi\,\mathsf{round}((\sqrt{5}-1)/4, r)$ for various r, where $\mathsf{round}(x, r)$ rounds x to r decimal places. We found that if we dramatically round the value of the irrational multiple of π to one or two decimal places, the behaviour of the resulting autocorrelations does not resemble the (fully) irrational case. This fact is expected as we are essentially simulating a rational triangular billiard with D, the smallest common denominator of

the angles, about 30 if we round to two decimal places. When we then consider rounding to larger number of decimal places, D increases dramatically. For example, if we consider the GM-GM triangular billiard with angles rounded to four decimal places, the corresponding D is about 3000. The resulting behaviour is then very similar to that found in the simulations without any rounding, see Figure 3.3, which means that in the case of asymmetric triangular billiards, all autocorrelations show signs of decay. Moreover, the autocorrelations computed using the rand method for the rounded angles and for the full angles are almost identical. While the shape of the autocorrelation function computed using the cuts method differs between the rounded and full cases, they both decay.

In the symmetric case, we observe a different behaviour between the autocorrelations for the rounded case for the cuts and rand methods, in line with observations presented in Chapter 5. This difference in the behaviour of the autocorrelation function is one of the reason why we are extra transparent about the details of our numerical simulations.

Overall, the autocorrelation functions computed for the rounded case both in the symmetric and asymmetric cases showcase the same type of behaviour as those computed for the 'full' case.

We include this section only as a justification of our simulations and, thus, will not elaborate on the reasons for the aforementioned behaviours at this stage.

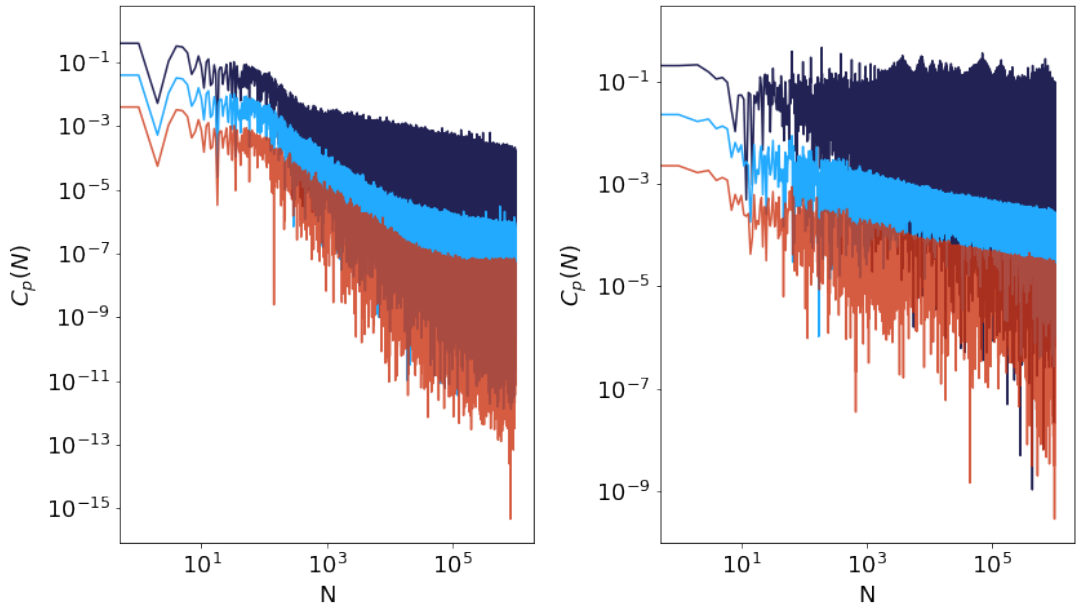

Figure 3.3: Autocorrelation functions of momentum for the SM-GM (left) and GM-GM (right) triangular billiards as a function of N, plotted on a double logarithmic scale. Dark blue lines in both panels correspond to autocorrelations computed using the cuts method for angles rounded to four decimal places, light blue lines correspond to autocorrelations computed using rand method for angles rounded to four decimal places. Red lines correspond to results computed using rand method for angles without any rounding. Light blue and red lines have been shifted by a factor of 10^{-1} and 10^{-2} respectively for visibility reasons. All autocorrelation functions were computed using orbits of length 2^{30} and averaging over an ensemble of size 10^3.

Part II

Irrational triangular billiards

Chapter 4

Asymmetric case

In contrast to rational triangular billiards, there was only limited mathematical progress for their irrational counterparts. Recent results, mainly published in the physics literature, are entirely based on numerical simulations, see *e.g.* [2, 10]. The few rigorous result are for 'typical' polygonal billiards [4, 12, 32], except for [50, 51] which is dealing with a special case of right-angled triangular billiard and we will discuss it further in Chapter 7. Numerical results indicate that general irrational billiards are ergodic with respect to Lebesgue measure, in line with rigorous results (*cf.* [32, 50, 51]), while the correlation decay indicates weak or even strong mixing, see [11, 26]. Some authors study a simplified model of the billiard map, *e.g.* [11, 26], with their results confirming the previous numerical findings. However, some recent results ([53, 54]) are in conflict with these previous findings. Another fact to consider is that it is not always completely obvious how the results were obtained and, therefore, it is nearly impossible to reproduce them. Overall, the picture for general irrational triangular billiards is not entirely consistent. On one hand, the mathematical literature provides few rigorous results, often for a generic set-up, which are somewhat difficult to apply to a specific case. On the other hand, results in the physics literature provide data for a specific system but without any proof. Notably, limitations of numerical simulations due to slow correlation decay might

present an issue for the study of polygonal billiards.

In this and the following chapters, it is my goal to present clear and concise results which are reproducible. Therefore, all algorithms used are described in Chapter 2, while the code can be found on `https://github.com/katz313/Triangular-Billiards`. This chapter is based on [54]. We use the same notation as in Chapters 1 and 2.

This chapter is organised as follows. The main results, demonstrated on one particular example of the SM-GM triangular billiard, are presented in Section 4.1, while an overview of other triangular billiards we have considered is in Section 4.2.

4.1 Main results

For our investigations we consider the billiard map T using Birkhoff coordinates (s, p) as defined in Chapter 1. As the goal is to investigate (weak) mixing, the quantity of interest is the autocorrelation function of an observable f given by

$$C_f(n) = \langle f \cdot f \circ T^n \rangle_\mu - \langle f \rangle_\mu^2 ,$$

where $\langle \dots \rangle_\mu$ denotes the average with respect to a $T-$invariant measure μ (see Section 1.2 of Chapter 1 for details). Mixing requires correlation functions to decay for all μ-square-integrable observables f, while weak mixing requires only the Cèsaro sequence associated to the absolute value of the autocorrelation function of the observable f, $\frac{1}{N}\sum_{n=0}^{N-1} |C_f(n)|$, to decay for any μ square integrable observable f. However, due to the nature of the numerical simulations, it is only possible to check the behaviour of a few observables and hope that the findings are generic. As explained earlier in Chapter 1, our chosen observables are the momentum p and the cyclic position observable defined as $\zeta(s) = \sin(2\pi s/L)$, where L denotes the circumference of the triangle.

Although we will illustrate all the relevant points on the SM-GM triangular billiard, all other investigated asymmetric irrational triangular billiards exhibit the same general

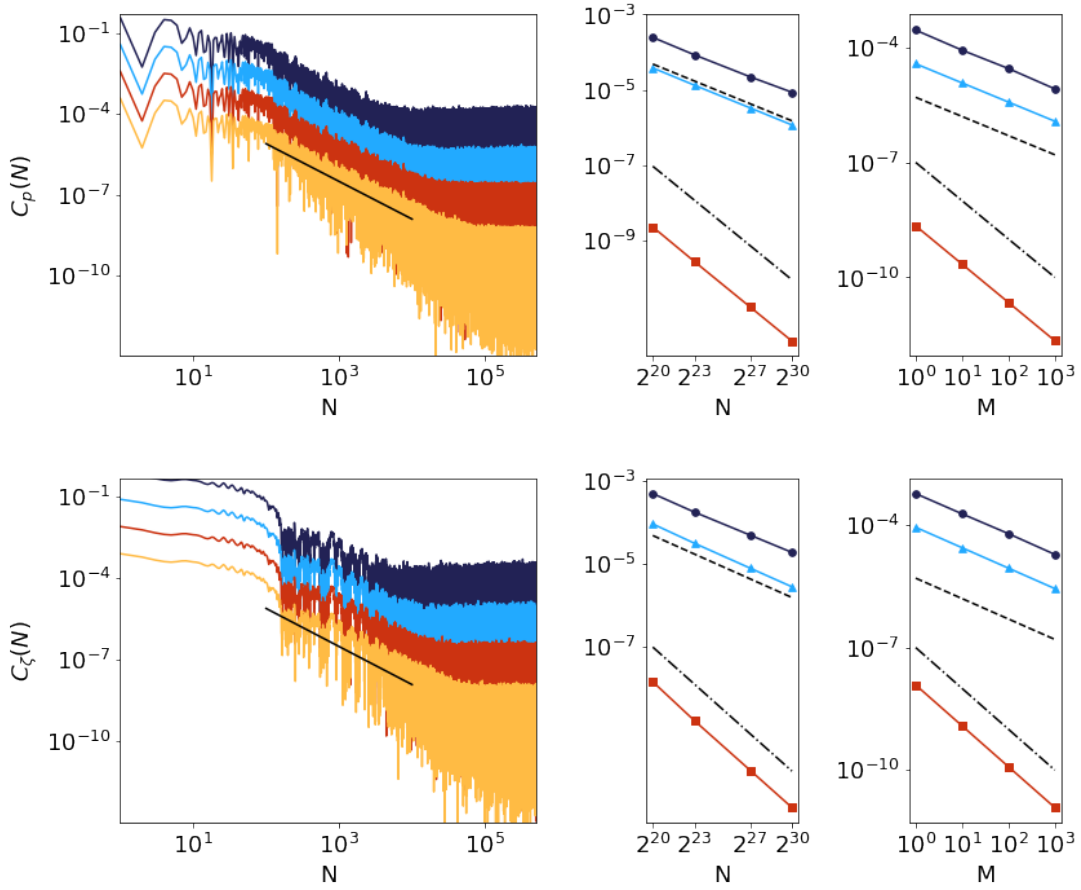

Figure 4.1: Upper panel: data for the momentum p. Lower panel: data for the cyclic position observable ζ. Both panels are organised as follows:
Left: Autocorrelation function on a double logarithmic scale for the SM-GM triangle. Data has been computed for a time series of length 2^{30} with ensemble sizes as follows: $N = 1$ (dark blue), $N = 10$ (light blue), $N = 10^2$ (red), and $N = 10^3$ (yellow). For visibility reasons, values have been shifted by a factor of 10^{-1}. The full black line indicates a power law decay with exponent -1.41 (upper panel) and -1.45 (lower panel), following the results in Table 4-A.
Middle: The dependence of the plateau value for large time as a function of the time series length. The maximum (dark blue circles) and the absolute mean (light blue triangles) follow a power law decay with exponent 1/2 (dashed), whereas the variance (red squares) decays as a power law with exponent 1 (dash-dotted).
Right: The dependence of the plateau value for large time (time series length of 2^{30}) as a function of the ensemble size. The maximum (dark blue circles) and the absolute mean (light blue triangles) follow a power law decay with exponent 1/2 (dashed), whereas the variance (red squares) decays as a power law with exponent 1 (dash-dotted).

behaviour. The only quantity which differs is the speed of the decay, see Section 4.2 for details.

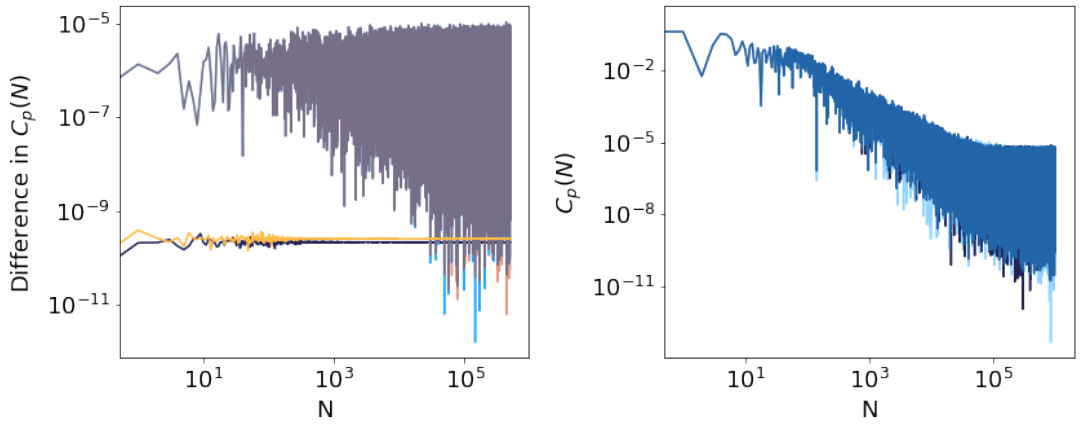

Figure 4.2: Figure comparing the different methods of computing the autocorrelation function of momentum used in the asymmetric case. Orbits of length 2^{30} were used, along with 10^3 ensembles.
Left: differences of discounted cuts and non-discounted cuts method (dark blue), and discounted rand and non-discounted rand method (yellow). Comparison of the discounted cuts and discounted rand method (light blue), and the discounted cuts and non-discounted rand method (transparent red).
Right: the autocorrelation function of momentum computed using the cuts (dark blue) and rand (light blue overlay) method.

The autocorrelation functions computed by our approach show a power law decay as N increases, see Figure 4.1, indicating strong mixing. The exponent of the power law shows a weak dependence on the observable and considerably stronger dependence on the angles of the triangular billiard, see Table 4-A. Autocorrelations level off at large time scales, with the concrete times of levelling off varying depending on the particular triangular billiard and the observable. The large time plateau values scale with both the orbit and sample size (see middle and right panels of Figure 4.1 consistent with that for sum of independent random numbers. Therefore, we are confident that this levelling off is caused by sampling errors due to finite sample sizes.

The effect of using a different method of computation of the autocorrelation function is illustrated in Figure 4.2. The difference between discounted and non-discounted autocorrelation function is negligible for both the cuts and the rand method. As for a comparison between the computation methods, their difference stays more or less constant and, as can be seen from the right panel of Figure 4.2, the overall shape of the

autocorrelation function is the same. Therefore, the fact that the size of this difference between the computational methods is considerably larger of that between discounted and non-discounted autocorrelations computed using the same method stems from the oscillations in the autocorrelation itself. Overall, the data clearly indicates that the behaviour of the autocorrelation function is the same regardless of the method used to compute it.

4.2 Summary of asymmetric triangular billiards

While only results for the SM-GM triangular billiard were presented in the previous section, triangular billiards with different angles were considered. As discussed in Section 1.4, we tried to choose our angles in a way to encompass different number theoretical properties of the irrational numbers. Although the exact behaviour of the autocorrelation functions vary depending on the chosen triangular billiard and observable, all of the combinations we considered demonstrate a similar overall behaviour with a power law decay with levelling off at large time scales. The following table and figure summarise our findings.

	C_p	C_ζ
SM-GM	-1.41	-1.45
PiPi-Log3	-0.98	-1.02
PiPi-GM	-1.11	-1.10
SQ2-PiPi	-1.20	-1.21
SM-PiPi	-1.46	-1.20
SQ2-SQ3	-0.97	-0.95

Table 4-A: Table of exponents of the power law decay of autocorrelation functions for different asymmetrical irrational triangular billiards. Slopes have been calculated for non-discounted autocorrelation functions computed for orbits of length 2^{30}, averaged over ensemble size of 1000, using the `rand` method. All values were rounded to two decimal places. Slopes were calculated using linear regression from the `scikit-learn` library and are accurate to two decimal places.

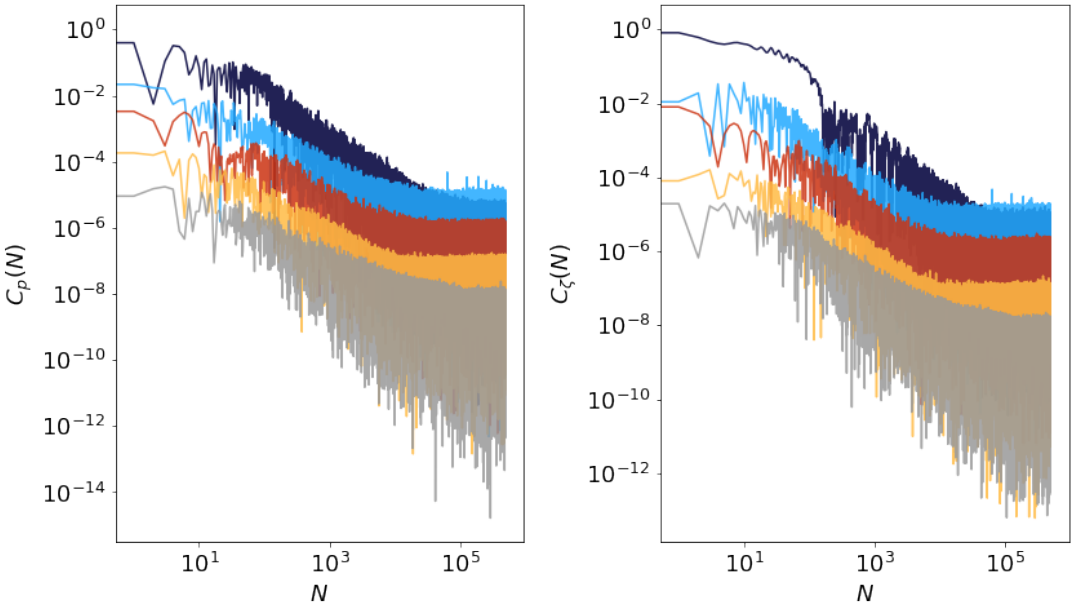

Figure 4.3: Autocorrelation functions of momenta p (left) and the cyclic position ζ for different triangular billiards. All autocorrelations were computed using the non-discounted rand method from orbits of length 2^{30} and averaged over ensemble size 1000. The colour coding is as follows: SM-GM (dark blue), PiPi-GM (light blue), SM-PiPi (red), SQ2-PiPi (yellow), SQ2-SQ3 (grey).

Chapter 5

Symmetry and its breaking

Whereas our results for the asymmetric billiards are not particularly surprising, the situation is different in the symmetric case. By the seminal result of [32], Lebesgue measure is ergodic for triangular billiards for a large set of angles, when the property being a large set is measured in topological terms. On one hand, the results of [2] and of the previous section indicate that this holds in typical numerical simulations. On the other hand, the question of ergodicity of a typical polygonal billiard is yet to be fully solved. For example, whether or not the set of ergodic billiards has a positive Lebesgue measure is still unclear [23]. However, the belief is that the Lebesgue measure is ergodic. In this chapter, we will present a wide array of data suggesting that Lebesgue measure may not be ergodic for symmetric triangular billiards, and, thus, that symmetric irrational triangular billiards may not belong to the large set of ergodic triangular billiards described in [32].

The chapter is organised as follows. Section 5.1 sets the scene with a brief discussion of phase portraits. Autocorrelation functions are discussed in Section 5.2. Section 5.3 introduces slightly asymmetric triangular billiards. An order parameter is introduced in Section 5.4. Section 5.5 deals with distribution of finite time ergodic averages, whereas convergence of ergodic average of momentum is discussed in Section 5.6. Lastly, a sum-

mary and a brief discussion can be found in Section 5.7. This chapter is based on [54].

5.1 Phase portrait conundrum

As already mentioned, majority of literature supports ergodicity of Lebesgue measure for most 'typical' triangular billiards, including the symmetric ones. It was, therefore, surprising that our numerical findings do not support this for symmetric triangular billiards. Before starting with a thorough examination of the symmetric case, let us begin the presentation of our results with a naive observation about phase portraits. Although phase portraits are not in themselves indicative of the overall dynamical behaviour, they provide a straightforward example of the difference in behaviour between the symmetric and asymmetric case.

As can be seen in Figure 5.1, although the phase space is populated in a more or less uniform fashion in the case of the asymmetric triangular billiard, the same is not true for the symmetric case. The dynamics in the symmetric triangular billiard even for long orbits is still confined to a set of lines. As the middle part of Figure 5.1 indicates, the orbit fails to properly reach the corner point corresponding to the obtuse angle. Moreover, the bottom part of that figure shows that only about 30% of the 600 possible bins corresponding to the different momenta are actually visited.

Although this observation is nowhere near conclusive, it provides us with an insight of the intricacies in the dynamics.

5.2 Autocorrelations

Another indication of different dynamical behaviour is the dependence of autocorrelation functions on the method of their computation. Whereas the autocorrelation behaved the same in the asymmetric case regardless of the chosen method (*cf.* Figure 4.2), the same is no longer true for symmetric triangular billiards. Here both the method of computation (the cuts or rand method) and whether the zero frequency is discounted or not play an

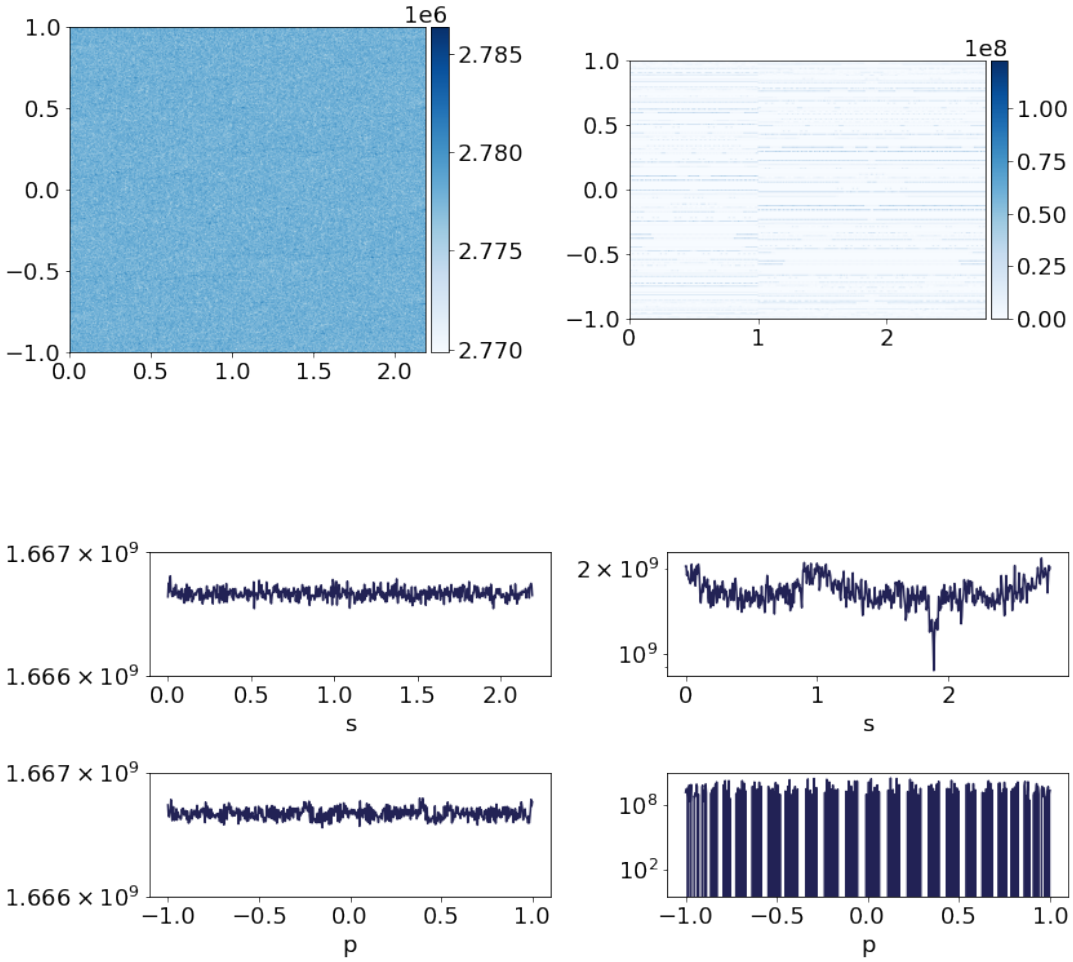

Figure 5.1: Top: Phase portrait comparing the asymmetric SM-GM triangular billiard (left) and symmetric GM-GM (right). Both phase portraits have been computed from an orbit of length 10^{12} as a histogram with bin size of order 10^{-3}, with the resolution of 600×600. The initial condition (s_0, p_0) has been kept the same for both triangles and is representative of all initial condition tested.
Middle: Total number of collisions occurring in interval $[s, s + \delta s)$, plotted on a semi-logarithmic scale. The asymmetric SM-GM triangular billiard is on the left, the symmetric GM-GM on the right. The drop in the symmetric case corresponds to the obtuse angle over the base.
Bottom: Total number of collisions occurring in interval $[p, p + \delta p)$, plotted on a semi-logarithmic scale. The asymmetric SM-GM triangular billiard is on the left, the symmetric GM-GM on the right. It is clear that the some values of the momenta p (about 70%) have not been visited at all in the symmetric case.

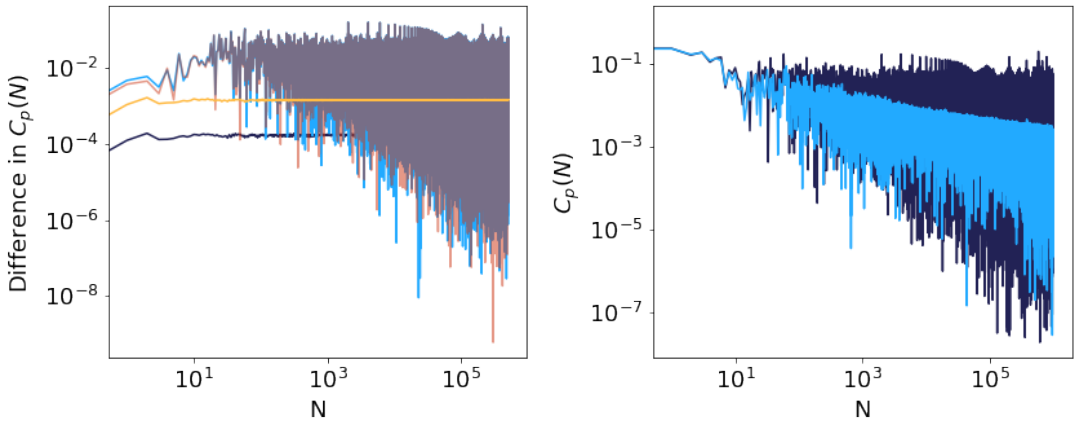

Figure 5.2: Figure comparing the different methods of computing the autocorrelation function of momentum used in the symmetric case. Orbits of length 2^{30} were used, along with ensembles of size 10^3.
Left: differences of discounted cuts and non-discounted cuts method (dark blue), and discounted rand and non-discounted rand method (yellow). Comparison of the discounted cuts and discounted rand method (light blue), and the discounted cuts and non-discounted rand method (transparent red).
Right: the autocorrelation function of momentum computed using the cuts (dark blue) and rand (light blue) method.

important role (see Figure 5.2).

In contrast to the asymmetric case, not only are the errors substantially larger but also the overall shape of the autocorrelation is different, as is evident from the right part of Figure 5.2. Overall, if one is interested in investigating the autocorrelation functions of symmetric triangles, one needs to take extra care in choosing the computational method. This dependence of the result on the method of calculation is another indication that ergodicity of symmetric triangular billiards needs to be carefully investigated.

5.3 Slightly asymmetric triangular billiards

To better understand this strange behaviour observed in the case of symmetric triangular billiards, we introduce a parameter ε to break the symmetry and observe the results. Hence, we included *slightly* asymmetric triangular billiards in our study of the dynamic behaviour. As stated in Section 1.4, by slightly asymmetric triangular billiards we mean

triangular billiards with angles α and $\beta = \alpha - \pi\varepsilon$ where ε is small. The original case of the symmetric triangular billiard then corresponds to $\varepsilon = 0$ and by increasing the parameter ε, we increase the asymmetry of the billiard table. By varying the size of ε, we can study the effect of the symmetry breaking on the overall behaviour.

As mentioned in Chapter 1, the angle of reflection φ changes linearly with the angles of the billiard in each collision. Thus, one might expect that it can take around $1/\varepsilon$ collisions for the triangular billiard to feel the slight asymmetry. This effect is demonstrated in Figure 5.4.

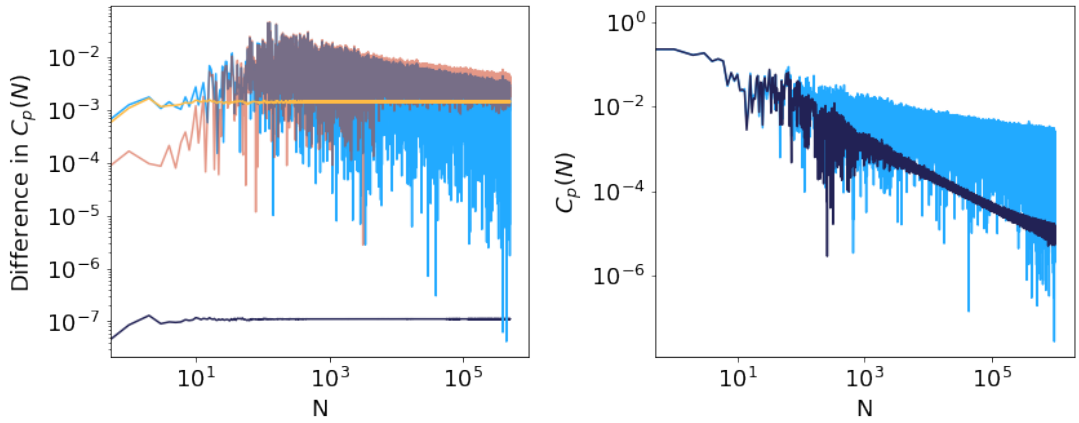

Figure 5.3: Figure comparing the different methods of computing the autocorrelation function of momentum used in the slightly asymmetric case. Orbits of length 2^{30} were used, along with ensembles of size 10^3.
Left: differences of discounted cuts and non-discounted cuts method (dark blue), and discounted rand and non-discounted rand method (yellow). Comparison of the discounted cuts and discounted rand method (light blue), and the discounted cuts and non-discounted rand method (transparent red).
Right: the autocorrelation function of momentum computed using the cuts (dark blue) and rand (light blue) method.

For the slightly asymmetric triangle, the autocorrelation functions behave similarly to symmetric triangular billiards in the sense that the value of the correlation function is dependent on the method of its computation (see Figure 5.3). The difference there, however, is that the autocorrelations decay regardless of the method — only the slope of the decay differs.

With this setup, we can investigate the ergodicity of the Lebesgue measure for symmetric triangular billiards.

5.4 Order parameter

A necessary condition for the ergodicity of the invariant measure μ is that the Cèsaro sequence associated to the autocorrelation function *i.e.*

$$\left(\frac{1}{N} \sum_{n=0}^{N-1} \langle f \cdot f \circ T^n \rangle_\mu - \langle f \rangle_\mu^2 \right) \to 0$$

decays to zero as $N \to \infty$ for any μ-square integrable observable f. As we are trying to discern whether Lebesgue measure is ergodic, we introduce the order parameter Φ_f for the observable f as

$$\Phi_f(N) = \frac{1}{N} \sum_{n=0}^{N-1} \langle f \cdot f \circ T^n \rangle_{\text{Leb.}} , \tag{5.1}$$

to measure ergodicity of the uniform distribution. The introduction of an order parameter is a well known technique from solid state physics to measure spontaneous symmetry breaking in phase transitions. If Lebesgue measure is ergodic then, using Theorem 1.2, we have $\lim_{N\to\infty} \Phi_f(N) = \langle f \rangle_{\text{Leb.}}^2$. By restricting our investigations to observables with vanishing Lebesgue average, $\langle f \rangle_{\text{Leb.}} = 0$, we can disprove ergodicity of Lebesgue measure by showing that $\Phi_f(N)$ does not vanish as $N \to \infty$. Note that for both of our chosen observables, the momentum p and the cyclic position ζ, the averages $\langle p \rangle_{\text{Leb.}}$ and $\langle \zeta \rangle_{\text{Leb.}}$ vanish. Numerical results were computed using Algorithm 6.

We compare the symmetric and slightly asymmetric cases for various values of ε to illustrate the effect of symmetry. Our findings do not substantially depend on the value of the angle α, that is, we observed qualitatively similar behaviour for other angles. The dependence of the order parameter for observables p and ζ on N can be found in Figure 5.4. Again, the overall behaviour does not seem to depend on the choice of the observable. In all the slightly asymmetric cases we simulated, the order parameter for both observables tends to zero, and this tendency becomes stronger as ε increases. This

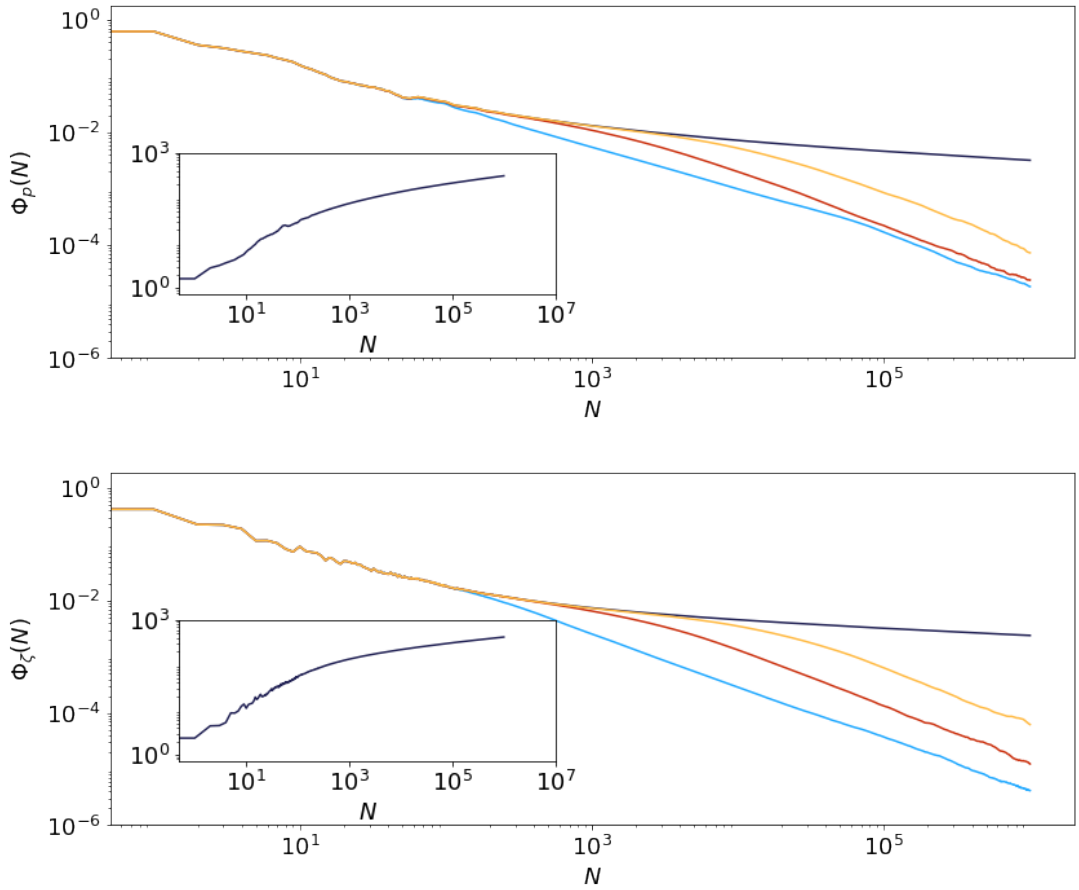

Figure 5.4: Order parameter as a function of N on double logarithmic scale for the symmetric GM-GM triangular billiard (dark blue), slightly asymmetric GM-GM billiards with $\varepsilon = 10^{-3}$ (light blue), 10^{-5} (red), and 10^{-7} (yellow). The top part corresponds to the momentum observable, the bottom panel to the cyclic position ζ. The insets show $1/\Phi_p$ and $1/\Phi_\zeta$ respectively. All autocorrelations were computed from orbits of length 2^{27} using the non-discounted rand method, averaged over 10^4 initial conditions.

supports ergodicity of Lebesgue measure in the case of slighly asymmetric triangles. On the other hand, the results for the symmetric case are not fully conclusive. The order parameters for both momentum p and cyclic position ζ have no clear limit. From the numerical data both order parameters could either tend to a finite value or they could tend to zero in extremely slow fashion, see insets in Figure 5.4. Overall, the behaviour of both order parameters supports ergodicity breaking of Lebesgue measure or, at the very least, point towards a very slow sub-logarithmic relaxation time scale, which is not possible to easily simulate in direct simulations. Either way, the numerical results clearly

indicate that the underlying dynamics in symmetric triangular billiards is different to the asymmetric case.

5.5 Distribution of ergodic averages

In order to further investigate this strange phenomenon, we evaluate the distribution of finite time averages

$$P_N(z) = \langle \delta(z - \bar{p}_N) \rangle_{\text{Leb.}} \tag{5.2}$$

where

$$\bar{p}_N = \frac{1}{N} \sum_{n=0}^{N-1} p \circ T^n \tag{5.3}$$

denotes the partial ergodic sum of momentum. If the system is ergodic with respect to Lebesgue measure, the distribution is expected to resemble the normal distribution. If that is not the case, then properties of the distribution (5.2) may help to identify different ergodic components of the system. Numerical results, computed using Algorithm 7, for both the symmetric and slightly asymmetric GM-GM triangular billiards are in Figure 5.5.

Again, there is a notable difference between the symmetric and slightly asymmetric case. The distribution for the slightly asymmetric triangular billiards shows scaling according to large deviation theory with $P_N \sim \exp\{-N\phi(z)\}$ and maximum and variance follow the law of large numbers with exponential tails. Moreover, we can again observe the effect of the size of the asymmetric parameter ε - the more asymmetric the triangular billiard is, the better it follows the aforementioned scaling. In contrast, there is little to no scaling with N in the symmetric case. This could point towards a flat non-equilibrium potential and many ergodic components which the uniform distribution in composed of. Overall, this is further evidence of possible non-ergodicity of Lebesgue measure for the case of symmetric triangular billiards.

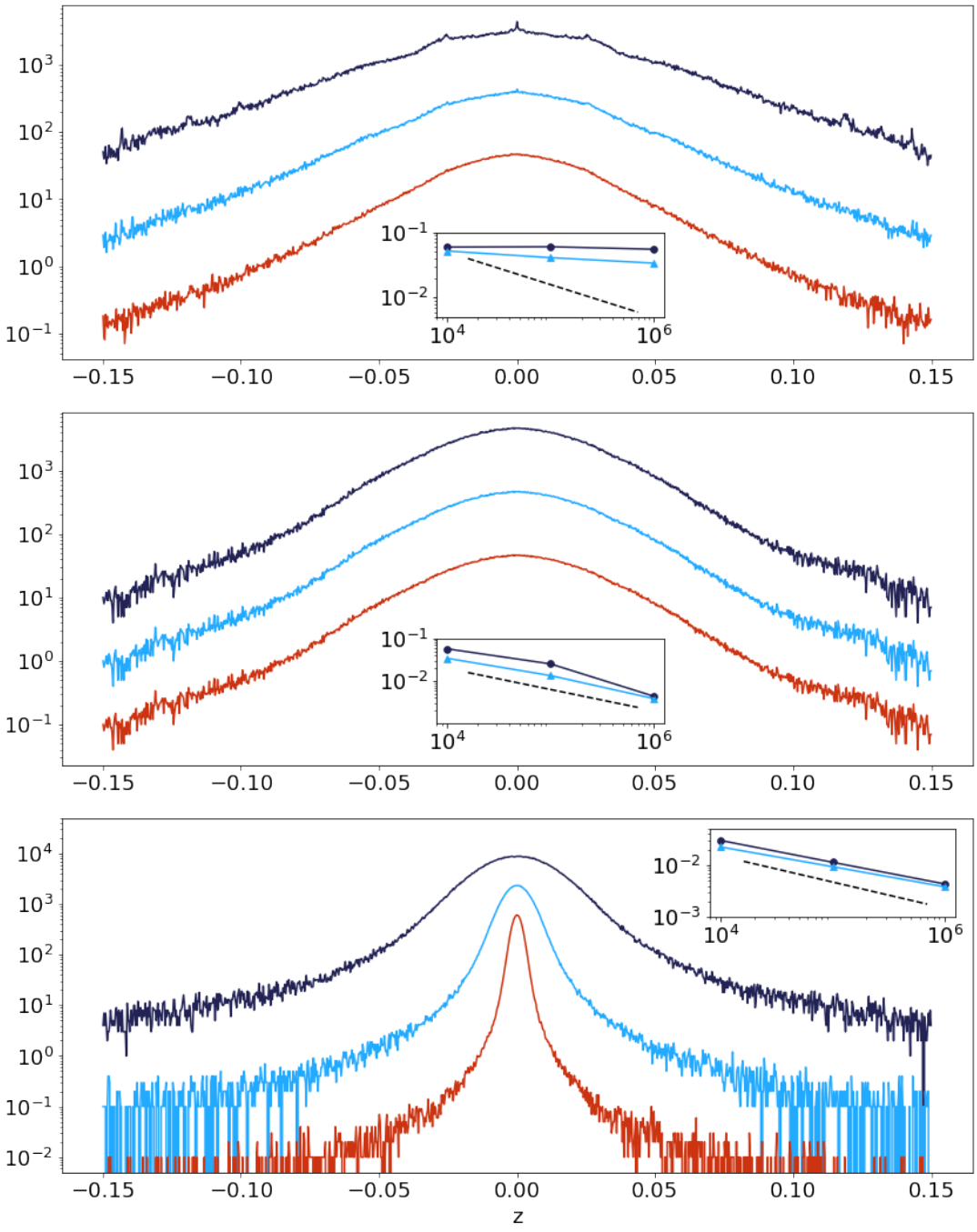

Figure 5.5: Distribution of the finite time ergodic average of momentum p, see equation (5.2), on a semi-logarithmic scale. Top lines (dark blue) correspond to $N = 10^4$, middle lines (light blue) to $N = 10^5$, and bottom lines (red) to $N = 10^6$ iterations. Data have been computed from a uniform random ensemble of initial conditions with ensemble size 10^6. The distributions have been generated as a histogram with bin size 4×10^{-4}. The insets show the half-width (dark blue circles) and standard deviation (light blue triangles) for the three values of N, along with the trivial scaling $1/\sqrt{N}$ (dashed).
Top: symmetric GM-GM triangular billiard
Middle: slightly asymmetric GM-GM triangular billiard with $\varepsilon = 10^{-5}$,
Bottom: slightly asymmetric GM-GM triangular billiard with $\varepsilon = 10^{-3}$.

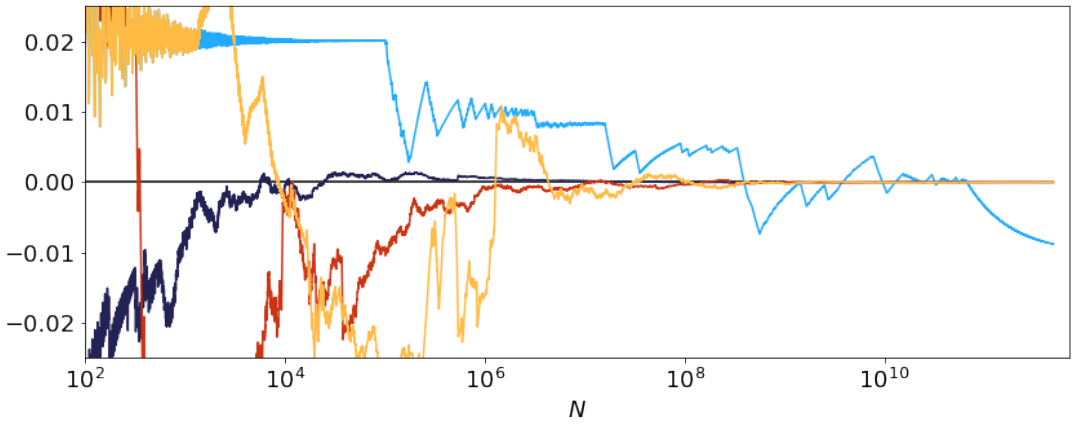

Figure 5.6: Ergodic averages of momentum, see equation (5.3), on a semi-logarithmic scale, for an asymmetric SM-GM (dark blue), a symmetric GM-GM (light cyan), slightly asymmetric GM-GM triangular billiards with $\varepsilon = 10^{-3}$ (red) and $\varepsilon = 10^{-7}$ (yellow). All orbits were computed for a fixed initial condition $(s_0, p_0) = (0.5, 0.64)$

5.6 Ergodic averages of momentum

Our last argument for the non-ergodicity of Lebesgue measure for symmetric triangular billiards has to do with the convergence of the ergodic averages of momenta. We evaluate point-wise convergence of individual ergodic averages, see equation (5.3) and Algorithm 8, for given initial value (s_0, p_0). Although results vary depending on the choice of the initial condition, the overall behaviour is similar and the results presented in Figure 5.6 are representative of all initial conditions we investigated. In the asymmetric and slightly asymmetric case, ergodic averages converge to the analytic value $\langle p \rangle_{\text{Leb.}} = 0$, in line with ergodicity of the uniform distribution. For the slightly asymmetric triangular billiards, the speed of convergence is dependent on the size of ε, as expected. This effect can be observed on the red and yellow lines in Figure 5.6. In stark contrast, in the symmetric case, ergodic averages may not even converge. Instead, behaviour of the ergodic average is remarkably similar to that found in stable heteroclinic networks [3, 25, 35], where the dynamics is dominated by exponentially increasing sticking times to saddle points. In these cases symmetry plays a crucial role as well.

5.7 Summary

We have provided compelling numerical evidence that symmetry of triangular billiards plays a crucial role for the ergodic properties of the dynamics. While correlations with respect to Lebesgue measure appear to decay for typical irrational triangular billiards, the uniform distribution does not even appear to be ergodic in case of symmetric triangular billiards. We showcase the effect of symmetry by comparing the dynamical behaviour of symmetric and slightly asymmetric triangular billiards. The potential non-ergodicity of Lebesgue measure has been pointed out recently [53] without reference to the underlying symmetry of the system. The importance of symmetry, on the other hand, is also mirrored by a toy model of the triangle map, see [11], showing similar features to our findings to the symmetric and asymmetric dichotomy. Finally, symmetry turns out to be relevant when rational billiards are considered and where better analytical insight can be gained. While the uniform distribution is not ergodic in these cases, one observes very slow convergence of ergodic averages when isosceles rational triangles with large denominators are investigated. All in all, these findings support the claimed dichotomy between symmetric and asymmetric triangular billiards.

Effects of symmetry will be investigated further in the next chapter.

Chapter 6

Right-angled triangular billiards

In the last chapter, we presented substantial evidence that symmetry plays a crucial role in the dynamical behaviour of triangular billiards. We expand on this observation in this chapter, where we present results concerning right-angled triangular billiards, which are closely related to the symmetric case. If one unfolds the dynamics of a right-angled triangular billiard at one of the catheti, one obtains the dynamics in a symmetric triangular billiard with an *almost* two-to-one correspondence (explained further in Section 6.1) between the orbits of both systems [55]. Although there is no obvious relation between the ergodic properties of both systems, one would expect that the dynamics in both triangular billiards are closely related. Over the years, right-angled triangular billiards have been the most studied special case of irrational triangular billiards. There are results suggesting ergodicity of Lebesgue measure, weak mixing but not mixing ([2]), results claiming non-ergodicity for a large number of angles α [53], and extremely slow diffusion [27]. Hence we revisit the problem in this chapter, presenting results of our numerical simulations, and comparing the behaviour of right-angled, symmetric, and asymmetric triangular billiards.

The organisation of this chapter is as follows. In the first section we explain in more detail the relationship between the right-angled and the symmetric case, including the

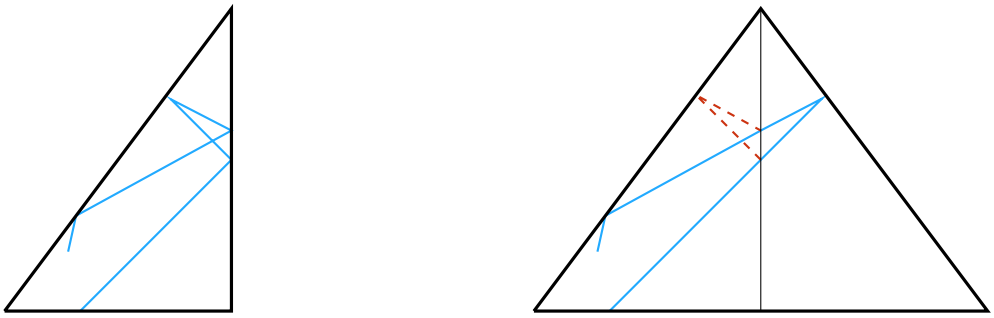

Figure 6.1: Unfolding of right-angled triangular billiard into a symmetric one. An orbit originating from the same initial condition is plotted to compare its behaviour.

process of unfolding and orbit correspondence. Section 6.2 includes several subsections with numerical results using the same tests as in Chapter 5. Results for other triangular billiards with exactly one rational angle are presented in Section 6.3. We discuss our findings in the last section. This chapter is partially based on [54].

6.1 Unfolding of right-angled triangles

When one investigates the dynamics of symmetric triangular billiards, a natural follow up question is what happens in the right angled case. Given a symmetric triangular billiard with angles α, α, and $\pi - 2\alpha$, we call a right-angled triangular billiard with angles α, $\pi/2$, and $\pi/2 - \alpha$ the *corresponding* right-angled triangular billiard. Even though the two systems are clearly related by unfolding (Figure 6.1), the relationship of their dynamic properties is sadly not as straight-forward.

As can be seen from Figure 6.1, the vertical wall adds complexity to the dynamics of right-angled triangular billiard. Whereas we plotted only three collisions for the light blue orbit in the symmetric case, the same part of the corresponding orbit (*i.e.* same momentum, scaled position) in the right-angled case contains five collisions.

Further investigation of the proportion of collisions happening on the vertical side brings a rather surprising discovery that the angles of the triangular billiard play a vital role. While there is a weak dependence on the choice of initial condition, the dependence on the angle is stronger, see Table 6-A for details.

α	$\bar{m}$	σ
SM	0.143	0.007
Log3	0.286	0.007
GM	0.345	0.003
SQ2	0.384	0.002
PiPi	0.416	0.001
SQ3	0.447	0.002

Table 6-A: Table summarising the proportion of collisions occurring on the vertical wall for different right-angled triangles. The angles have been ordered by their size in an increasing order. The mean $\bar{m}$ and the standard deviation of the proportion were calculated using 10 different orbits starting from uniformly distributed random initial conditions, each of length 10^9. We expect that the difference between the SM-Pi2 triangular billiard and the rest is due to the size difference in the angles. The proportions of collisions are stable under changes of orbit length and initial conditions.

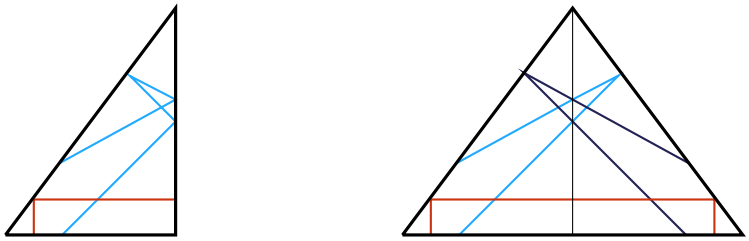

Figure 6.2: Illustration of the *almost* two-to-one correspondence of orbits in the right-angled and symmetric triangular billiard. From the original light blue orbit in the right-angled case, we are able to construct two orbits in the symmetric triangular billiard (light and dark blue). However, there is only one orbit corresponding to the red orbit in the right angled case.

Further more, there is the question about the *almost* two-to-one correspondence of orbits. Given an orbit in the right-angled triangular billiard, we are usually able to construct two orbits in the corresponding symmetric triangular billiard. One just by keeping the initial starting point in the left hand side of the triangle and the other by reflecting the position along the vertical wall and switching the sign of momentum. However, this construction fails for certain orbits. One such example is given in Figure 6.2. Hence, we talk about the *almost* two-to-one correspondence of orbits.

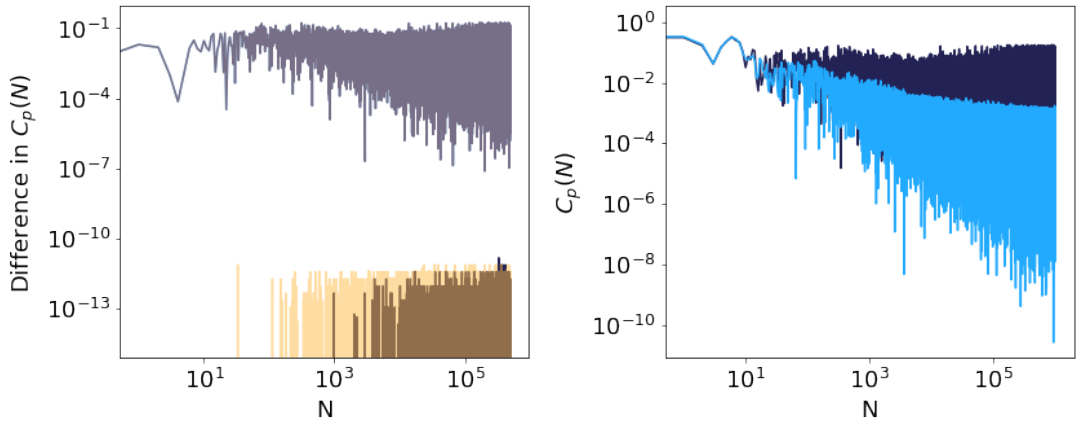

Figure 6.3: Comparison of autocorrelation function of momentum for the SM-Pi2 right-angled triangular billiard, computed using different methods. We used orbits of length 2^{30} and ensembles of size 10^3.
Left: difference of discounted and non-discounted cuts (dark blue) and rand (transparent yellow) methods. Comparison of discounted cuts and rand method (transparent red), and the non-discounted cuts and rand method (light blue).
Right: the autocorrelation function of momentum computed using non-discounted cuts (dark blue) and non-discounted rand (light blue) method.

6.2 Numerical results

Even though there is *almost* two-to-one correspondence between the orbits of both systems, there is no obvious relation between their dynamical properties. We performed the same tests on the right-angled triangular billiards as we did in the symmetric case in previous chapter. The following subsections present the corresponding results and compare them to that of a symmetric triangular billiard.

6.2.1 Autocorrelations

Similarly to the symmetric case, the autocorrelation function differs depending on the method of computation (see Figure 6.3). While the autocorrelations computed using the cuts method do not decay, the autocorrelations computed using the rand method show weak signs of decay, although the decay is much less pronounced than in general asymmetric triangular billiards. However, in contrast to the symmetric case, the difference between the discounted and non-discounted result of a single method is negligible.

6.2.2 Order parameter

The complexity added by the vertical wall is even more pronounced when we look at the behaviour of the order parameter Φ_f for observable f as defined in previous chapter in equation (5.1). There, we observed that neither the autocorrelation function (when computed using the cuts method) nor the order parameter decays in the case of symmetric triangular billiards. So far, we presented evidence that neither do the autocorrelation functions (computed using the cuts method) for the right-angled triangular billiard decay. However, as Figure 6.4 demonstrates, the order parameter Φ_p for the momentum observable p decays in the right-angled case, with the decay as strong as in the case of generic asymmetric triangular billiards. On the other hand, the order parameter Φ_ζ associated to the cyclic position observable ζ shows behaviour similar to that of symmetric triangular billiards.

6.2.3 Distribution of finite time ergodic averages

Whereas the behaviour of autocorrelation functions and of order parameters stands somewhere in between the asymmetric and symmetric case, the distribution of finite time ergodic averages of momentum, see Eq. (5.2), behaves qualitatively the same as for general asymmetric triangular billiards. Figure 6.5 show the distribution P_N for our choice of right angled triangular billiards — the SM-Pi2, GM-Pi2, and PiPi-Pi2 triangular billiards. As can be seen from the insets, both the half-width and standard deviation scale as $P_n \sim \exp\{-N\phi(z)\}$, in line with our expectations.

Following the unexpected behaviour of the order parameter Φ_ζ, we present the distributions of finite time ergodic averages of the cyclic position observable ζ in Figure 6.6. Again, here we see a similar type of behaviour to the case of the ergodic sums with respect to momentum of symmetric triangular billiards, *cf.* Figure 5.5. Overall, while the behaviour of ergodic averages of momentum supports the ergodicity of Lebesgue measure, the situation with the cyclic position is not as clear.

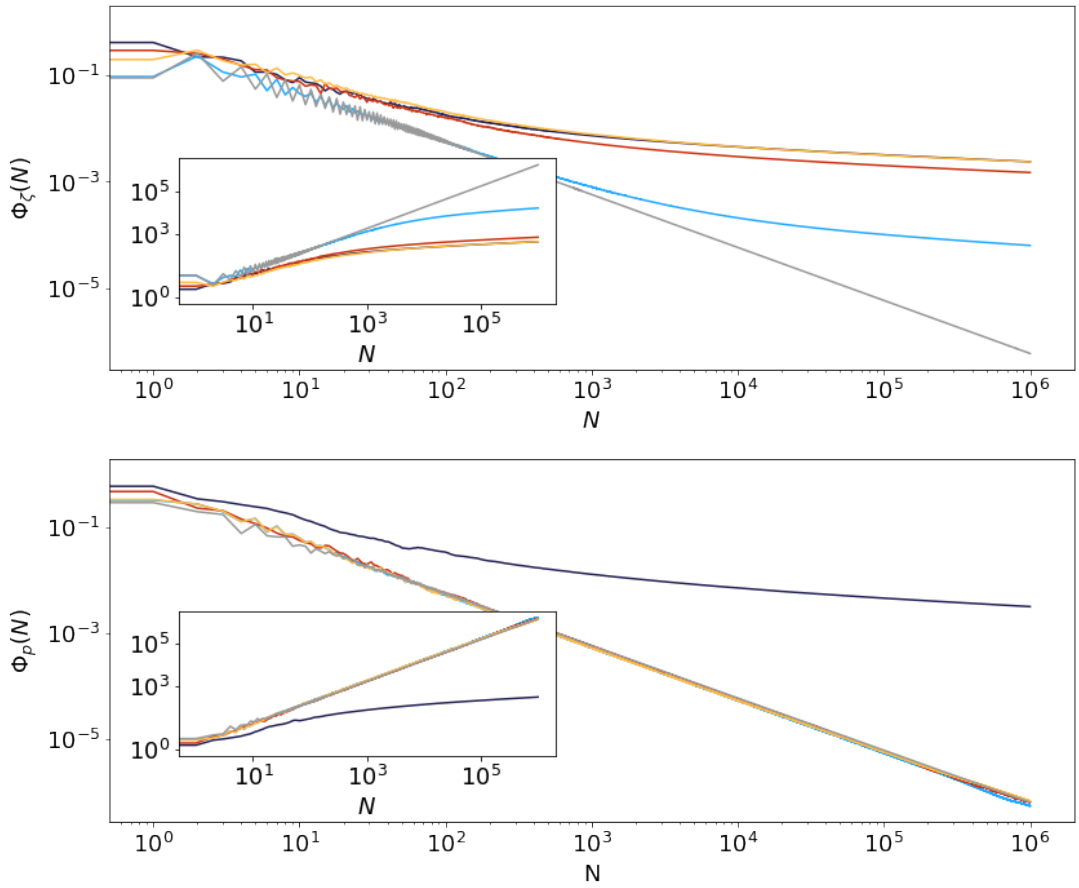

Figure 6.4: Order parameter as a function of N on a double logarithmic scale for SM-Pi2 (light blue), GM-Pi2 (red), PiPi-Pi2 (yellow) right angled triangular billiards, symmetric GM-GM (dark blue), and asymmetric SM-GM (grey) triangular billiards for comparison. Top part corresponds to momentum and bottom to the cyclic position observable ζ. The insets show $1/\Phi_p$ and $1/\Phi_\zeta$ respectively. All autocorrelations were computed from orbit of length 2^{27} using the non-discounted rand method, averaged over 10^4 initial conditions.

6.2.4 Convergence of ergodic averages

Lastly, we present results concerning the convergence of ergodic averages of momentum, see equation (5.3) and Algorithm 8 for more details. Again, here we see a strong resemblance to the general asymmetric behaviour, with the ergodic average converging to the analytical value $\langle p \rangle_{\text{Leb.}} = 0$ at the same rate or even quicker than in some general asymmetric cases. Although the exact convergence shows a weak dependence on both the angles of the billiard and on initial condition, all variations of both decayed to 0 at at most the same rate as in general asymmetric triangles.

6.3 Comparison with other triangular billiards

We include this section in order to compare the behaviour of right-angled triangular billiards to that of other irrational billiards with exactly one angle being a rational multiple of π. In the previous section we presented results indicating that the ergodic behaviour of right-angled triangular billiards is somewhere in between that of symmetric and asymmetric ones. However, we have yet to present any evidence that this is due to the special connection between the right-angled and symmetric case and not due to the fact that one of the angles is a rational multiple of π. Therefore, we shall now compare the behaviour of the order parameters Φ_p and Φ_ζ for the right-angled case with triangular billiards with angles $\pi/3$ and $\pi/4$. As can be seen from Figure 6.8, in all cases we simulated, the order parameters decay, with the speed of the decay weakly dependent on the angles in the billiard. Interestingly, there is a slight difference in the speed of decay for the two order parameters. While the order parameter in triangles with angle $\pi/3$ decay a bit faster in case of the cyclic position observable ζ, billiards with the angle $\pi/4$ exhibit faster decay for the momentum order parameter. Overall, the speed of decay for both order parameters is reasonably similar to that of a generic asymmetric irrational triangular billiard. More importantly, we do not observe any suspicious levelling off as in both the symmetric and right-angled cases.

6.4 Discussion

While there is an obvious geometric relationship between symmetric and right-angled triangular billiards, this does not fully translate to their respective dynamical properties. On one hand, we presented compelling evidence for non-ergodicity, or at least extremely large relaxation time scales, of the Lebesgue measure in the symmetric case. On the other hand, data for the right-angled triangular billiards are not fully conclusive. While the distribution and convergence of ergodic averages of momentum support ergodicity, the behaviour of autocorrelation functions as well as that of the order parameters lie somewhere in between generic asymmetric and symmetric triangular billiards. Overall,

the results indicate that while the symmetric and right-angled triangular billiards are related by the simple process of unfolding, further subtleties play an important role for their ergodic properties. We support this argument by showing that the order parameter behaves as expected for other triangular billiards with exactly one rational angle, therefore, the fact that the triangular billiard is not fully irrational does not seem to play a role. This further showcases the rich dynamical properties of triangular billiards.

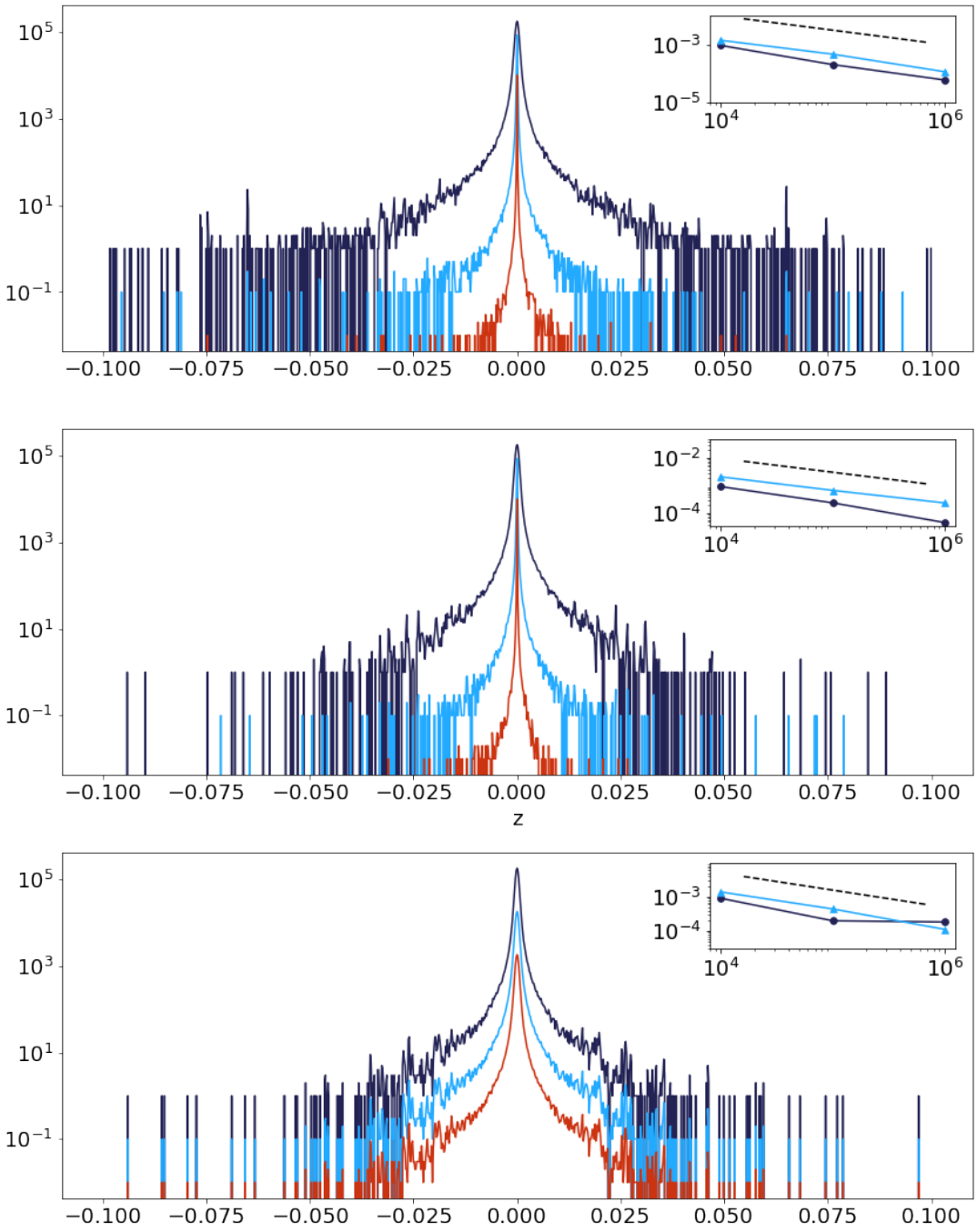

Figure 6.5: Distribution of the finite time ergodic average of momentum p, see equation (5.2), on a semi-logarithmic scale. Top lines (dark blue) correspond to $N = 10^4$, middle lines (light blue) to $N = 10^5$, and bottom lines (red) to $N = 10^6$ iterations. Data have been computed from a uniform random ensemble of initial conditions with ensemble size 10^6. The distributions have been generated as a histogram with bin size 2×10^{-4}. The insets show the half-width (dark blue circles) and standard deviation (light blue triangles) for the three values of N, along with the trivial scaling $1/\sqrt{N}$ (dashed).
Right-angled triangular billiards considered are as follows: SM-Pi2 (top), GM-Pi2 (middle), and PiPi-Pi2 (bottom).

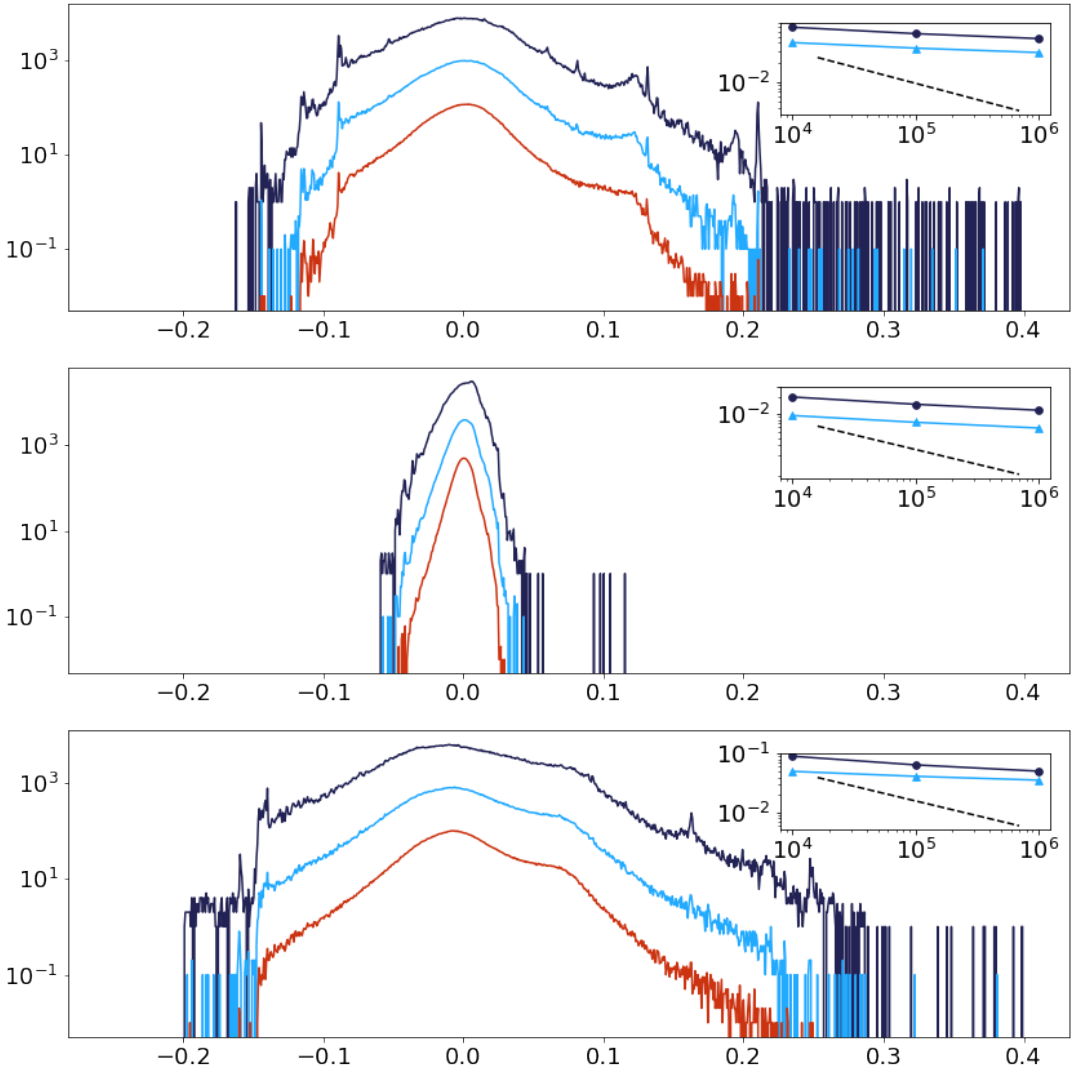

Figure 6.6: Distribution of the finite time ergodic average of the cyclic position observable ζ, Top lines (dark blue) correspond to $N = 10^4$, middle lines (light blue) to $N = 10^5$, and bottom lines (red) to $N = 10^6$ iterations. Data have been computed from a uniform random ensemble of initial conditions with ensemble size 10^6. The distributions have been generated as a histogram with bin size 2×10^{-4}. The insets show the half-width (dark blue circles) and standard deviation (light blue triangles) for the three values of N, along with the trivial scaling $1/\sqrt{N}$ (dashed).
Right-angled triangular billiards considered are as follows: SM-Pi2 (top), GM-Pi2 (middle), and PiPi-Pi2 (bottom).

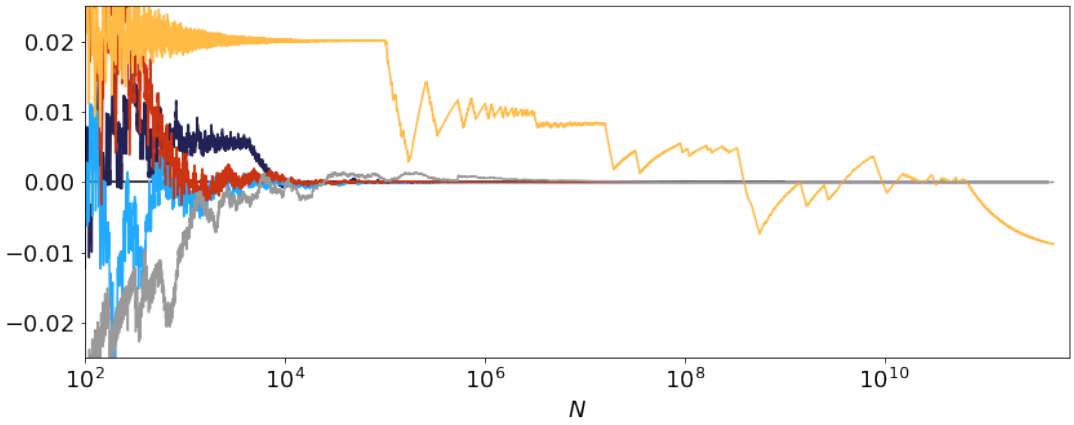

Figure 6.7: Ergodic averages of momentum, see equation 5.3, on a semi-logarithmic scale, for asymmetric SM-GM (grey), symmetric GM-GM (yellow), and right SM-Pi2 (dark blue), GM-Pi2 (light blue), PiPi-Pi2 (red) triangular billiards. All orbits were computed for same fixed initial condition $(s_0, p_0) = (0.5, 0.64)$.

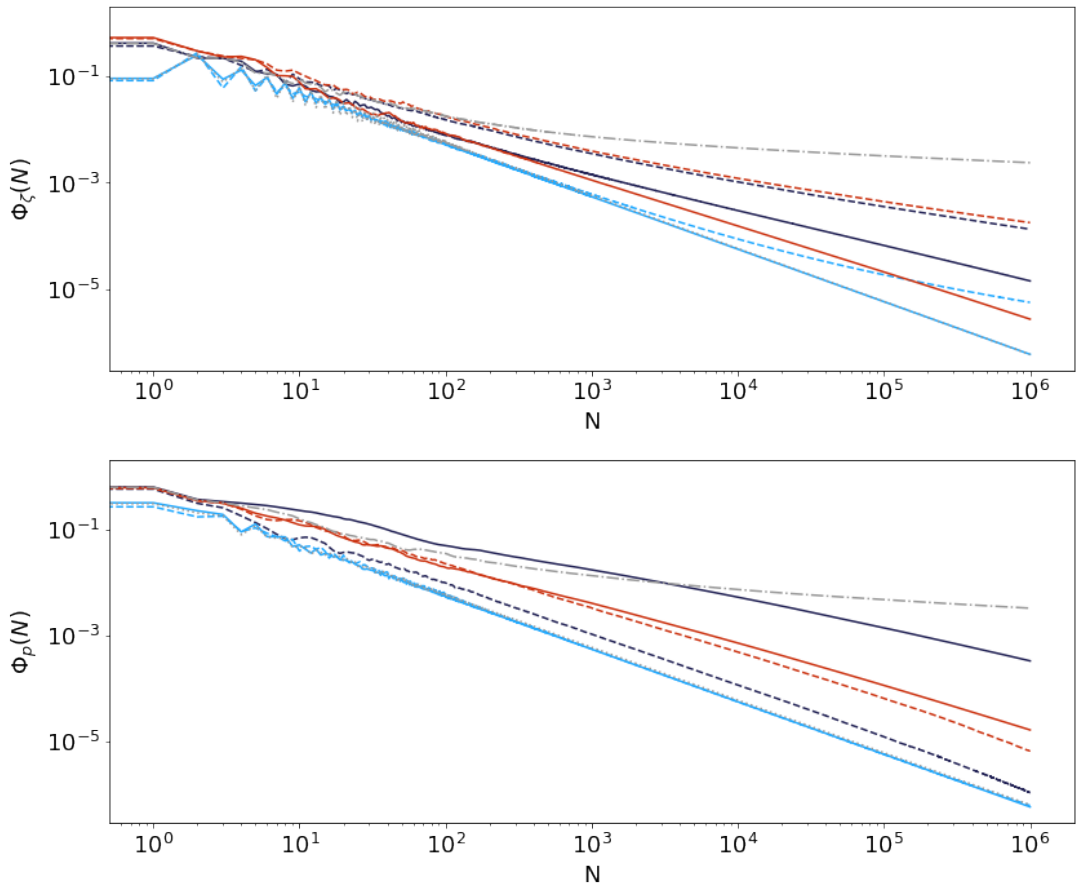

Figure 6.8: Order parameter Φ_ζ (top) and Φ_p (bottom) as a function of N, for GM-PiX (dark blue), SM-PiX (light blue), and PiPi-PiX (red) billiards, where Pi3 is plotted as a solid and Pi4 is dashed. We also plotted the asymmetric SM-GM (dotted grey) and symmetric GM-GM (dash-dotted grey) triangular billiards for comparison. All autocorrelation functions were computed from orbits of length 2^{27} using the non-discounted rand method, averaged over 10^4 initial conditions. Note that several lines overlap, especially in the order parameter of momentum Φ_p.

Chapter 7

Thin triangular billiards

In this chapter, we present our findings about thin triangular billiards. Our study of the thin case is motivated by the only explicit example, [50], found in the literature. In this paper, the author was able to prove ergodicity of Lebesgue measure for the billiard flow in a special right-angled triangular billiard, where one of the angles is a sum of so-called Liouville numbers. Due to the extremely small size of this special angle, it is impossible to accurately simulate such triangular billiard numerically. Therefore, we set upon studying triangular billiards that have at least one angle very small. We do not restrict our study to only right-angled triangles. On the contrary, the thin set up offers another opportunity to observe the effects of symmetry on the dynamical behaviour of the billiard.

This chapter is organised as follows. Section 7.1 introduces our notation and explores what we mean by a *thin* triangular billiard. Section 7.2 investigates phase portraits of various thin triangular billiards. A study of time spent in different sections, along with the upper bound for the number of collisions, can be found in Section 7.3. Autocorrelation functions are presented in Section 7.4.

7.1 How thin is thin

For our purposes, we define our triangles using rational multiples of the angles discussed in Section 1.4, *e.g.* GM/d for increasing d. With this construction, we are able to systematically investigate the effect of 'squishing' of the triangular billiard.

When deciding how *thin* a triangular billiard needs to be so that we call it thin, we considered the behaviour of phase portraits, more specifically the appearance of elliptical shapes (see next section for more details). Observing the changes in the phase portraits for different angles, we found that angles smaller than 0.15 usually foster the appearance of these elliptical shapes. A summary of angles used along with their respective size can be found in Table 7-A.

SM	0.3253	GM	0.9708
SM/5	0.0650	GM/5	0.1942
SM/35	0.0093	GM/35	0.0277
SM/50	0.0065	GM/50	0.0194

Table 7-A: Table of angles used in simulations for thin triangular billiards, rounded to 4 decimal places.

One reason why thin triangular billiards exhibit special behaviour is due to the effect that the change in momentum has on the next collision. While in a 'normal' triangular billiards, a substantial change in momentum results in a substantial change in the position of the next collision, the same is not true for their thin counterparts. This is due to the very short distance between the sides adjacent to the thin angle, hence the variation in direction does not result in a substantial change in the position of the next collision, see Figure 7.1. This makes the particle spend a long time in the thin part of the triangle, as there needs to be a large number of collisions in order to leave the thin leg. We investigate the numbers of collisions in the legs further in Section 7.3.

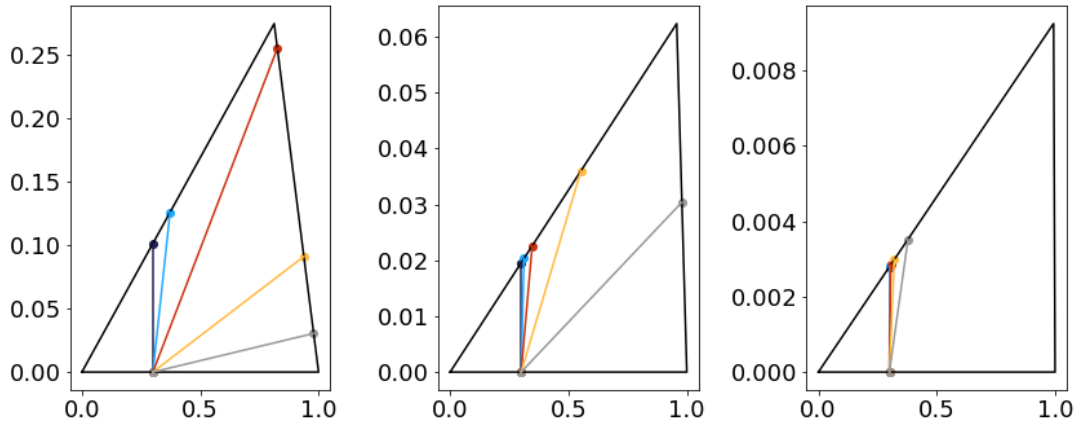

Figure 7.1: Illustration of how decreasing the angles in the triangular billiard affects orbits with different momenta. Orbits in all three billiards start at the same position $s = 0.3$ with momenta $p = 0$ (dark blue), $p = 0.5$ (light blue), $p = 0.9$ (red), $p = 0.99$ (yellow), and $p = 0.999$ (grey). Triangular billiards have angles as follows: SM-GM (left), SM/5-GM (middle), SM/35-GM (right).

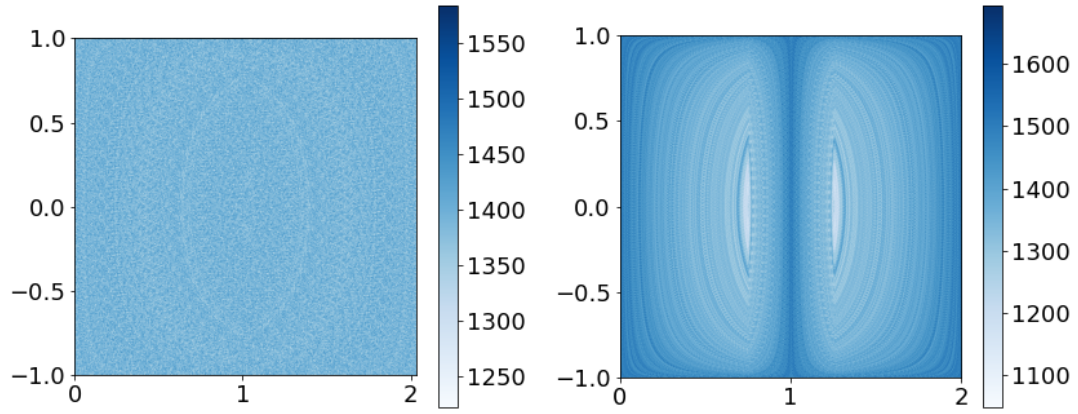

Figure 7.2: Phase portraits for the SM/5-GM/5 triangle (left) and the SM/35-GM/35 triangle (right). Both were computed as a histogram with bin width 5×10^{-3} for 3×10^{8} collisions starting from the same initial condition.

7.2 Elliptical shapes in the phase space

When considering the phase space for thin triangular billiards, a fixed initial condition produces ellipse-like shapes in the phase portrait. The effect emerges even for not so thin triangles (see Figure 7.2) and becomes stronger as the triangle flattens out. This has to do with the dynamics in thin cones, which we shall focus on presently.

Consider the following example of a thin cone with angle α and a particle starting from the horizontal side with initial condition $(s, \cos\varphi)$, see Figure 7.3.

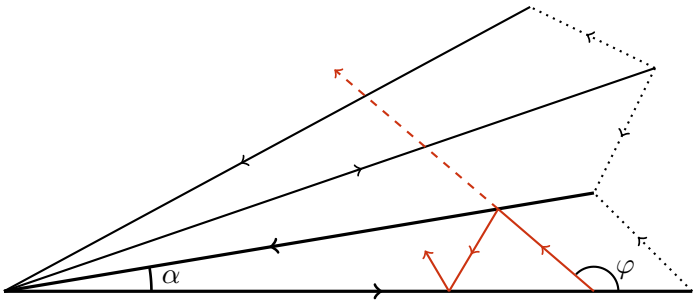

Figure 7.3: Unfolding of a thin cone with angle α. An orbit starting with angle φ is depicted within the cone (red, solid) and on the unfolding (red, dashed). The other side of the triangular billiard, not used in the unfolding, is dotted.

Using simple trigonometric identities, we find that the subsequent bounces have the following Birkhoff coordinates

$$\begin{cases} p_{2n+1} = -\cos(\varphi - [2n+1]\alpha)\,, \\ s_{2n+1} = L - s\frac{\sin\varphi}{\sin(\varphi-[2n+1]\alpha)}\,, \end{cases} \qquad \begin{cases} p_{2n} \;\; = \cos(\varphi - 2n\alpha)\,, \\ s_{2n} \;\; = s\frac{\sin\varphi}{\sin(\varphi-2n\alpha)}\,, \end{cases} \tag{7.1}$$

for $n \in \mathbb{N}$, with even collision occurring on the horizontal side and odd on the slanted side. The parameter L corresponds to the perimeter of the billiard.

When plotting the orbit in the phase space, s and p correspond to the x, respectively y, axis. We then get the following analytical equations:

$$\frac{c^2}{x^2} + y^2 = 1 \quad \text{resp.} \quad \frac{c^2}{(x-L)^2} + y^2 = 1\,, \tag{7.2}$$

where $c = s\sin\varphi \in (0,1)$ codes the initial condition. An example of curves for Eq. (7.2) are plotted in Figure 7.4.

Note while the curves in Eq. (7.2) do not explicitly depend on the triangular billiard, respectively its angles α and β, the dependence on the angles plays a role in the number

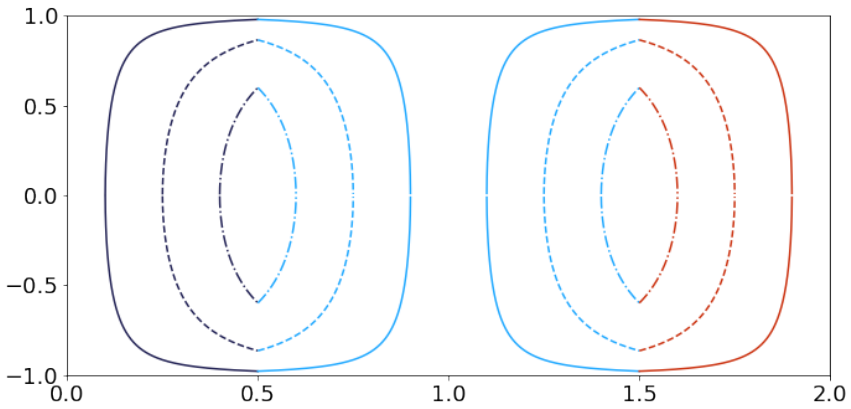

Figure 7.4: Curves from Eq. (7.2). Dark blue lines corresponds to $\frac{c^2}{x^2} + y^2 = 1$, red to $\frac{c^2}{(x-L)^2} + y^2 = 1$. Light blue corresponds to collisions in the right leg. The solid, dashed, and dash-dotted lines correspond to different initial conditions with $c = 0.1$, 0.25, and 0.4 respectively.

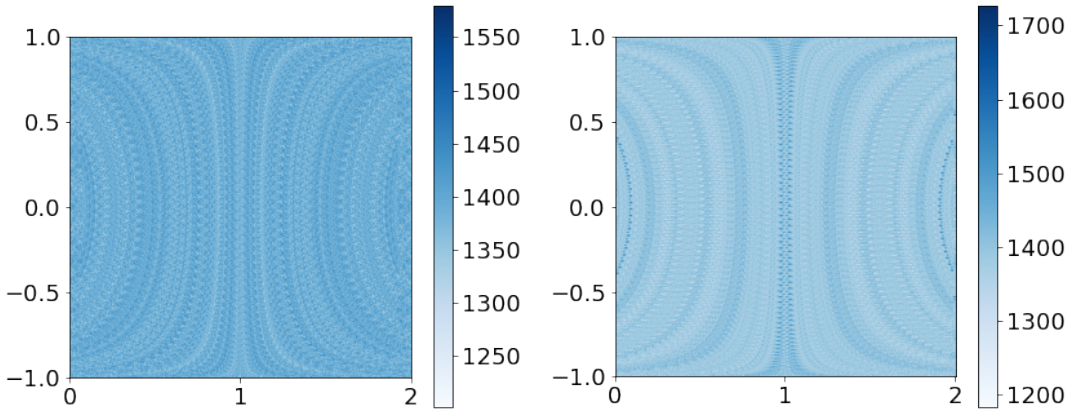

Figure 7.5: Phase portraits for the SM-GM/35 (left) and GM-GM/35 (right) triangular billiards. Both were computed as a histogram with bin width 5×10^{-3} for 5×10^8 collisions starting from the same initial condition.

of collisions in the respective legs – the smaller the angle, the denser the curves are 'sampled' in Eq. (7.2).

Finally, not only do elliptical shapes appear for triangular billiards where both angles are small, we observed similar type of behaviour in cases where just one angle was small, see Figure 7.5.

7.2.1 Stability of elliptical shapes

Even in the case of thin triangles, symmetric triangles behave differently to asymmetric ones. This can be observed in particular in the phase portraits, where the elliptical shapes slowly spread out to fill in the whole phase space for asymmetric thin triangular billiards. If we consider a histogram of the phase portrait in the thin asymmetric case with bin size of 3×10^{-3}, our simulations suggest that all bins have been visited after about 10^7 collisions. However, in the case of symmetric thin triangular billiards, the elliptical shapes seem to stop spreading after a certain number of collision, see Figure 7.6. Finally, while for asymmetric triangular billiards the elliptical shapes seem to fill the phase space in a continuous fashion, the phase space in the symmetric thin case does not appear to fill but keeps exhibiting non-uniformities with distinct stable line structure.

Of course, this is not a proof of non-ergodicity of the Lebesgue measure for the thin symmetric triangles, but gives us further evidence of a dichotomy in the behaviour of the two classes of irrational triangles.

To investigate this strange stability of ellipses further, we simulated the GM/35-GM/35 triangular billiard for several different initial conditions, varying the length of the orbit, while the resolution of the histogram is kept the same with bin size 3×10^{-3}. For all simulated initial conditions, the elliptical shapes stopped spreading for orbits of length between 10^{11} and 10^{12} collisions, more specifically, there were no newly visited bins when comparing histograms of the two lengths of the orbits. Two examples of the resulting phase portrait can be found in Figure 7.7.

While more investigation is needed, especially using greater resolution of the histogram, this (interim) stability presents further evidence of the difference in behaviour between symmetric and asymmetric triangular billiards.

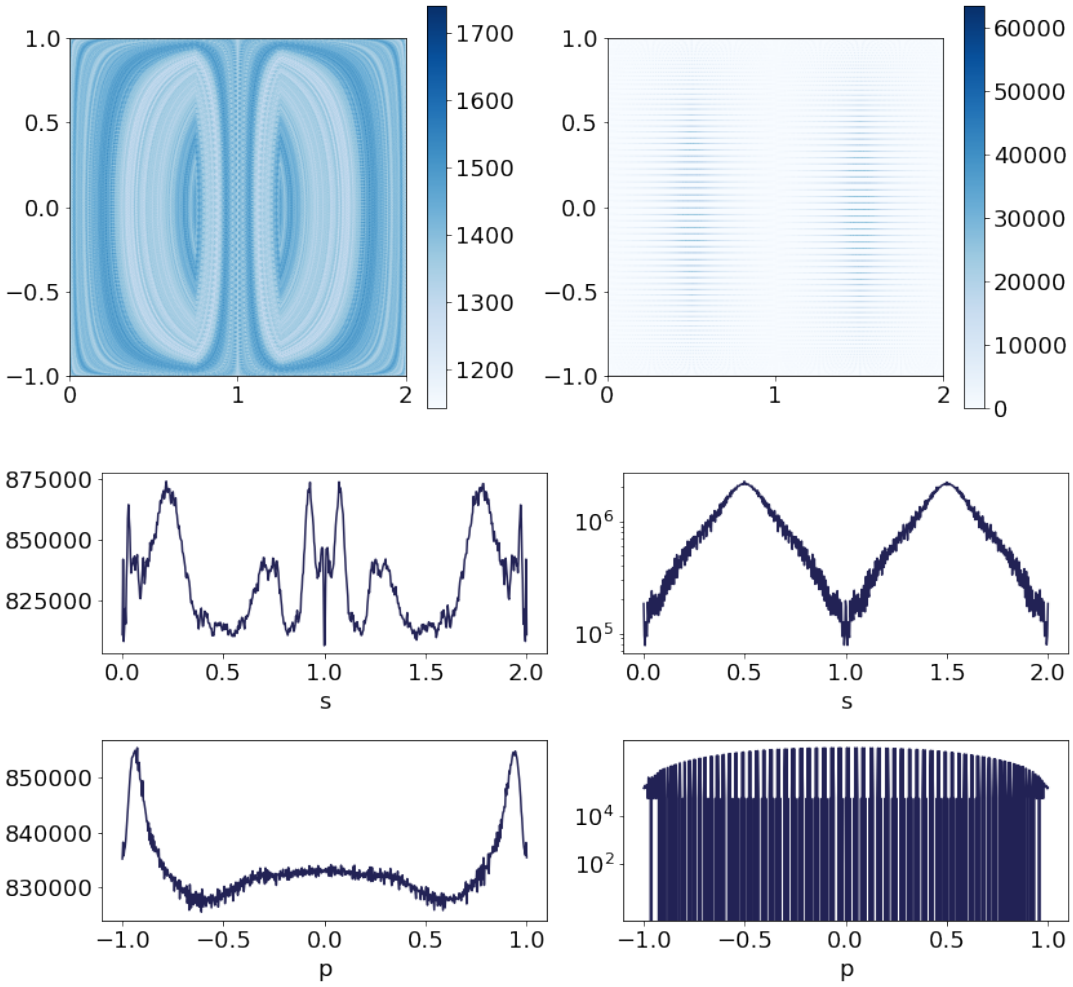

Figure 7.6: Top: Phase portraits for the SM/50-GM/50 triangle (left) and the GM/50-GM/50 triangle (right). Both were computed as a histogram with bin width 3×10^{-3} for 5×10^8 collisions starting from the same initial condition. Note that while every bin in the thin asymmetric triangle has been visited a number of times, most of the bins are empty in the symmetric case.
Middle: Total number of collisions with positional coordinate in the interval $[s, s + \delta s)$ obtained from the histogram above. The asymmetric SM/50-GM/50 triangular billiard is on the left, the symmetric GM/50-GM/50 on the right (plotted on a semi-logarithmic scale).
Bottom: Total number of collisions with positional coordinate in the interval $[p, p + \delta p)$ obtained from the histogram above. The asymmetric SM/50-GM/50 triangular billiard is again on the left, the symmetric GM/50-GM/50 on the right (plotted on a semi-logarithmic scale). Only about 47% of momenta intervals have been visited in the symmetric case.

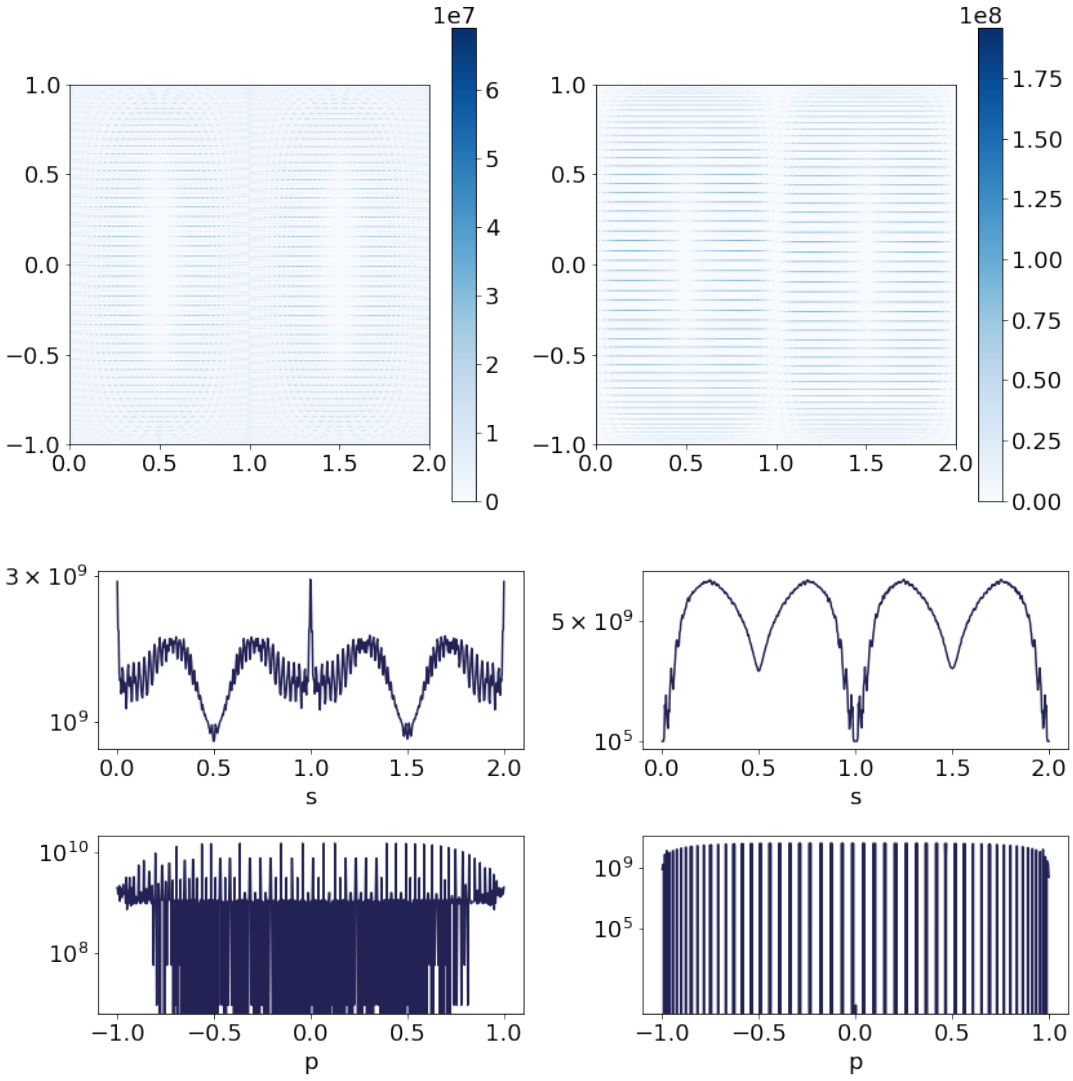

Figure 7.7: Phase portraits for GM/35-GM/35 triangular billiard, computed as a histogram with bin width 3×10^{-3} for 3×10^{12} collisions and two different initial conditions.
Middle: Total number of collisions with positional coordinate in the interval $[s, s + \delta s)$ obtained from the histogram above.
Bottom: Total number of collisions with positional coordinate in the interval $[p, p + \delta p)$ obtained from the histogram above, plotted on a semi-logarithmic scale. The total percentage of visited bins is 78% and 18% respectively.

7.3 Collisions in the legs

Next question we want to investigate is how the number of collisions in the legs changes. The Theorem 1.1 in Chapter 1 answered the question whether there is an upper bound on the number of collisions in an leg of a triangular billiard. Note that we can arrive at

the same answer by considering the maximum n such that $\varphi - 2n\alpha \in [0, \pi]$ in Eq. (7.1). Either way, we find that

$$N_{max}^{(\nu)} = \left\lfloor \frac{\pi}{\nu} \right\rfloor \tag{7.3}$$

is the maximum number of collisions in the leg with angle ν.

We can investigate how the number of collisions in the legs evolve over time and whether it reaches the maximum value N_{max}.

Again, there is a distinction between symmetric and asymmetric triangular billiards. This time, however, it is clearer that the symmetry plays a role as the maximum number of collisions is the same in both legs. Therefore, it is not altogether surprising that the number of collisions in thin symmetric billiards has a certain structure to it (see Figure 7.8). On the other hand, there is no reason why the maximum number of collision is rarely achieved in the symmetric case. Results indicate that this fact plays a role in the sparse 'sampling' of the elliptical shapes, resulting in more sparsely populated phase portraits. In the case of asymmetric thin triangular billiards, the number of collisions within the legs lacks any discernible structure but did not fail to reach maxima N_{max} for both legs in any situation we simulated.

7.4 Autocorrelations

Lastly, we present the results of autocorrelation computations. Again, there is a clear difference between symmetric and asymmetric triangular billiards, consistent with the results we obtained in the 'normal', non-thin, case (see Figure 7.9). For the simulations, we chose different combinations of angles from Table 7-A such that we could observe the effects of only one thin angle as well if there is a further effect of squishing the billiard. We computed the autocorrelations using both the cuts and rand methods, as well as checking the discounted and non-discounted versions of each. Overall, the one symmetric billiard we considered, GM/35-GM/35, was behaving very similarly to those symmetric billiards discussed in Chapter 5, *i.e.* there is a significant difference in autocorrelation functions

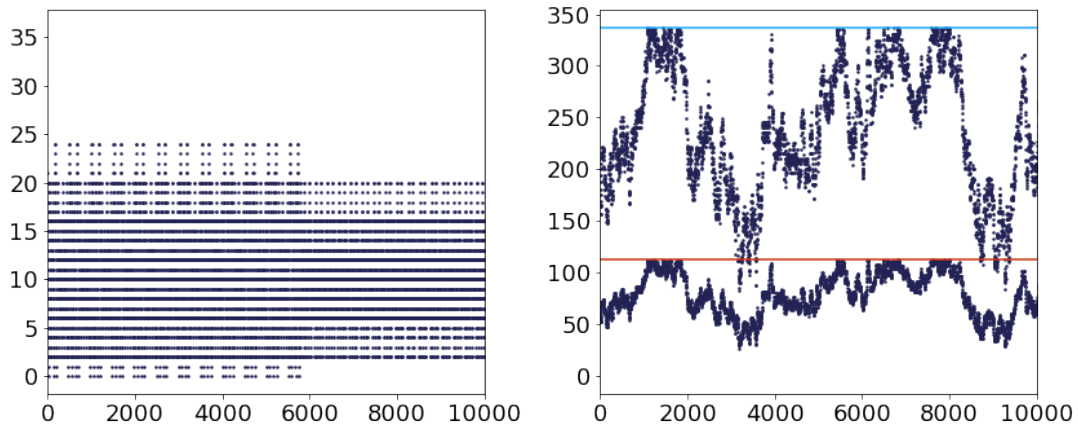

Figure 7.8: Number of collisions in the legs for the symmetric GM/35-GM/35 (left) and asymmetric SM/35-GM/35 (right) triangular billiards. Note that while the symmetric billiard on the left shows structure in the number of collisions in the two legs, the number of collisions does not approach $N_{max}^{(\mathrm{GM}/35)} = 113$. In the right pane, the number of collisions in the legs of the asymmetric billiard reaches both maxima, $N_{max}^{(\mathrm{GM}/35)} = 113$ (red line) and $N_{max}^{(\mathrm{SM}/35)} = 337$ (light blue line).

computed by the cuts and rand methods with less significant differences between the discounted and non-discounted versions of each. On the other hand, all the asymmetric thin triangular billiards we simulated show behaviour consistent with that of 'normal' asymmetric triangular billiards as presented in Chapter 4.

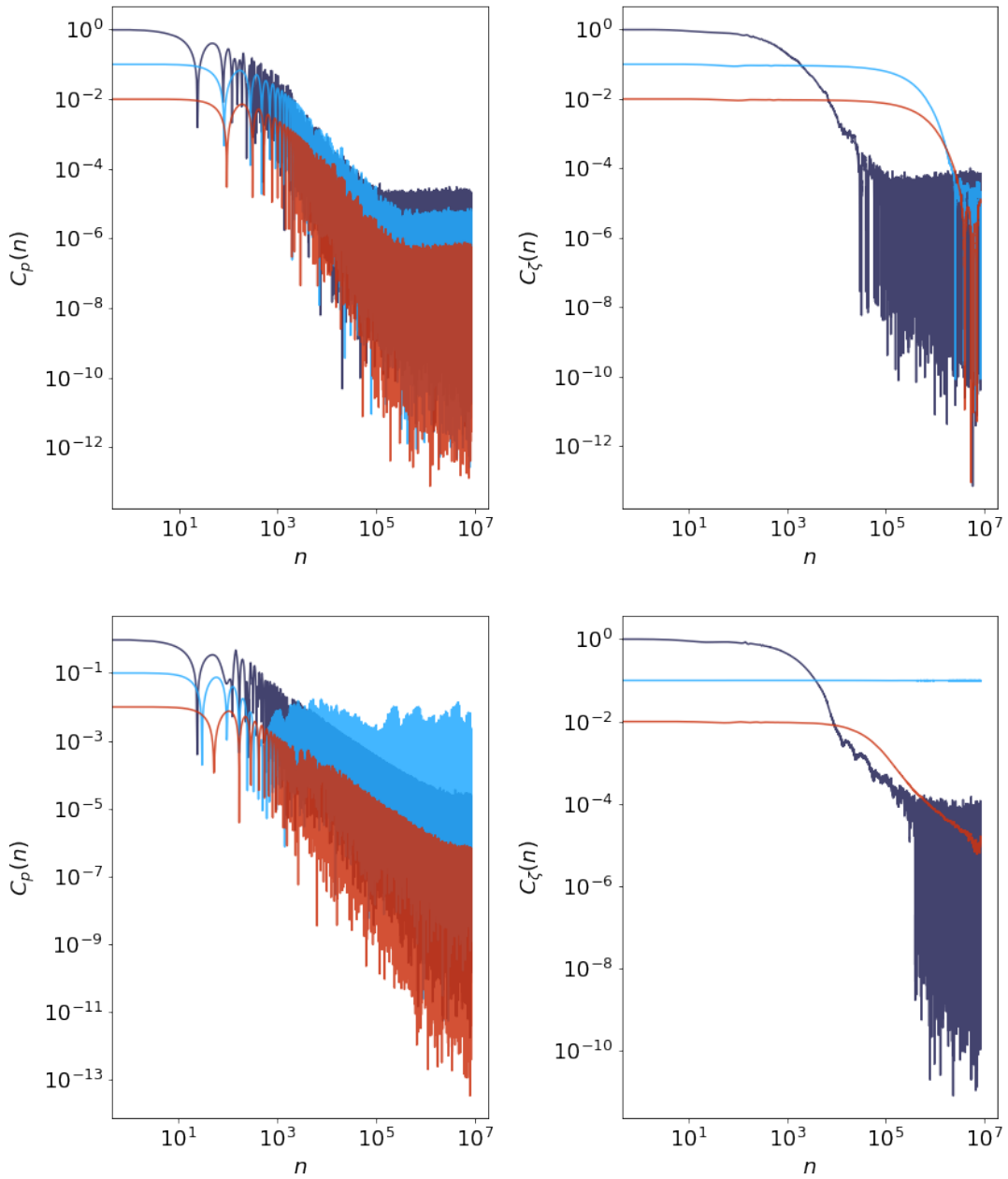

Figure 7.9: Autocorrelation functions of momentum p (left) and cyclic position observable ζ (right), plotted on a semi-logarithmic scale. We used the cuts method for orbits of length 2^{30} collisions, using ensembles of size 10^3. With the exception of the GM/35-GM/35 triangular billiard (red on bottom panel), all triangular billiards plotted are asymmetric.
Top: Autocorrelation functions for triangular billiards SM-GM/35 (dark blue), SM/35-GM/35 (light blue), and SM/35-GM/50 (red).
Bottom: Autocorrelation functions for triangular billiards GM-GM/35 (dark blue), GM/35-GM/35 (light blue), and GM/35-GM/50 (red).

Conclusion and outlook

In this thesis, we have focused on a numerical study of ergodic properties of triangular billiards. While there are substantial results in the mathematical literature for rational triangular billiards, there has been only limited progress in the case of their irrational counterparts. Most results regarding the dynamical behaviour of irrational triangular billiards come from the physics literature and are entirely based on numerical simulations. Moreover, these numerical results are frequently hard to interpret and replicate, as most authors do not explain in detail how the simulations were performed. Our approach, therefore, has been to provide numerical results together with a detailed explanation of the method of computation. We believe that greater transparency in the numerical methods is necessary as some results, *e.g.* autocorrelations, show considerable sensitivity to the method of calculation.

Our results from Chapter 4 aim to provide further evidence that 'typical' asymmetric irrational triangular billiards are mixing, while also presenting the algorithms used in Chapter 2 and discussing why we see the levelling out of autocorrelation functions. We acknowledge that these results, as all other results presented in this thesis, are only numerical in nature and, therefore, cannot answer the question of mixing in asymmetric triangular billiards for certain, as we were only able to study just a few observables in the case of just a few examples of such billiards. Furthermore, our implementation of irrational triangular billiards is only approximating the truly irrational case. Therefore, while our results may provide a good indication of the overall behaviour, they cannot be

fully conclusive.

Further, in Chapter 5, we have analysed the impact of symmetry of the billiard table on the system. We found compelling evidence that the dynamical behaviour of symmetric irrational triangular billiards is different to their asymmetric counterparts. The effect of symmetry was further illustrated by comparing the results for symmetric and slightly asymmetric triangular billiards. Our numerical results, performed using a range of different tests in several different settings, all indicate that Lebesgue measure may not be ergodic in the symmetric case. Autocorrelation functions depend on the method of computation and do not seem to decay, while order parameters have no clear limit. The distribution of finite time ergodic averages shows little to no scaling. And ergodic averages of momentum might not converge. Overall, we provided compelling numerical evidence that the dynamic behaviour of symmetric triangular billiards differs significantly from that of their asymmetric counterparts. Moreover, our results indicate that symmetric triangular billiards likely do not belong to the large set of triangular billiards that are ergodic with respect to Lebesgue measure as described in [32].

The effect of symmetry was investigated further in Chapter 6, where we have studied the ergodic properties of right-angled triangular billiards, which are closely related to the symmetric ones by the process of unfolding. Although the connection between right-angled and symmetric case seems simple, results of our numerical simulations indicate that their relation is not as straightforward. Similarly to the symmetric case, autocorrelations show dependence on the method of calculation and, generally, do not decay. The situation with the order parameter is, however, not as straightforward as its decay depends on the observable used in the computation. While the order parameter for the momentum observable decays as fast as in the case of asymmetric triangular billiards, the order parameter for the cyclic position observable ζ matches the behaviour of the symmetric case. In contrast, the order parameter for other triangular billiards with exactly one rational angle behaves similarly to the asymmetric case as expected. Finally, both the distribution and convergence of ergodic averages of momenta exhibits

behaviours of asymmetric triangular billiards. Overall, our results indicate that fully understanding the dynamical behaviour of right-angled triangular billiards is not as simple as one might think.

Lastly, we have focused on so-called thin triangular billiards in Chapter 7. This special class of triangular billiards exhibits interesting features in their phase portraits due to their shape. Even in this setting, results for symmetric triangular billiards differ from results for the asymmetric case.

Overall, we have presented convincing numerical evidence suggesting that symmetry plays a crucial role in ergodic properties of triangular billiards, although the exact mechanism remains unknown.

Future prospects

Lastly, we mention several potentially fertile areas of future research, which might provide further insight concerning the ergodic properties of triangular billiards with particular emphasis on effects of symmetry.

- ★ **Billiard flow** Many results in the literature are either for the billiard flow (*e.g.* [12, 32, 51]) or it is unclear whether the map or flow was used it the simulations. While ergodicity of the flow is equivalent to ergodicity of the billiard map (with respect to the same measure), it would be interesting to compare and contrast simulations of both as some tests may be better suited to either of those implementations. Therefore, contrasting the implementations of both the flow and the map could be useful in recovering further evidence for our results.

- ★ **Triangle map** Many results, *e.g.* [11, 26], are for the simplified model of the triangle map, instead of the full triangular billiard. It would be interesting to implement the triangle map and study the two systems together, searching for differences and similarities.

★ **Induced maps** Another possible way of studying triangular billiards would be to consider the induced map on the base of the triangle as well as replacing the momentum p for the angle φ as the coordinate of choice. One can easier study how the scattering angles evolve in different triangular billiards, as well a as study necessary conditions for recurrence of those angles.

★ **Special choices of angles** One might examine if choosing rationally related angles, *e.g.* $\alpha = 2\beta$, has any effect on the dynamical behaviour of the irrational asymmetric triangular billiards. While we performed similar tests in Chapter 7, choosing smaller rational multiples might produce interesting results, especially when studying the induced maps and recurrence.

★ **Effects of symmetry in the quantum case** Finally, studying specta of symmetric and asymmetric irrational triangular billiards in the quantum setting might provide further insight into the role of symmetry.

References

[1] R. Artuso. Correlations and spectra of triangular billiards. *Physica D: Nonlinear Phenomena*, 109(1):1–10, 1997. Proceedings of the Workshop on Physics and Dynamics between Chaos, Order, and Noise.

[2] R. Artuso, G. Casati, and I. Guarneri. Numerical study on ergodic properties of triangular billiards. *Physical Review E*, 55(6):6384–6390, June 1997.

[3] P. Ashwin and P. Chossat. Attractors for robust heteroclinic cycles with continua of connections. *Journal of Nonlinear Science*, 8(2):103–129, April 1998.

[4] A. Ávila and G. Forni. Weak mixing for interval exchange transformations and translation flows. *Annals of Mathematics*, 165(2):637–664, March 2007.

[5] V. Baladi. *Dynamical Zeta Functions and Dynamical Determinants for Hyperbolic Maps*. Springer International Publishing, 2018.

[6] G. D. Birkhoff. *Dynamical Systems*. American Mathematical Society / Providence, Estados Unidos. American Mathematical Society, 1927.

[7] M. Boshernitzan. A condition for minimal interval exchange maps to be uniquely ergodic. *Duke Mathematical Journal*, 52(3), September 1985.

[8] A. Boyarsky and P. Góra. *Laws of Chaos: Invariant Measures and Dynamical Systems in One Dimension*. Birkhäuser Boston, 1997.

[9] L. A. Bunimovich. *Dynamical systems, ergodic theory and applications*, pages 192–233. Encyclopaedia of Mathematical Sciences. Springer, Berlin, Germany, 2 edition, April 2000.

[10] G. Casati and T. Prosen. Mixing property of triangular billiards. *Physical Review Letters*, 83(23):4729–4732, December 1999.

[11] G. Casati and T. Prosen. Triangle map: A model of quantum chaos. *Physical Review Letters*, 85(20):4261–4264, November 2000.

[12] J. Chaika and G. Forni. Weakly mixing polygonal billiards. *arXiv e-prints*, March 2020.

[13] D. J. Chappell, D. Löchel, N. Søndergaard, and G. Tanner. Dynamical energy analysis on mesh grids: A new tool for describing the vibro-acoustic response of complex mechanical structures. *Wave Motion*, 51(4):589–597, June 2014.

[14] N. Chernov and R. Markarian. *Chaotic Billiards*. Mathematical surveys and monographs. American Mathematical Society, 2006.

[15] I. P. Cornfeld, S. V. Fomin, and Ya. G. Sinai. *Ergodic Theory*. Grundlehren der mathematischen Wissenschaften №245. Springer-Verlag New York, 1 edition, 1982.

[16] F. M. de Aguiar. Quantum properties of irrational triangular billiards. *Physical Review E*, 77(3):036201, March 2008.

[17] V. I. Arnold D.V. Anosov and S. P. Novikov Ya. G. Sinai, editors. *Dynamical Systems I-VIII. Encyclopedia of Mathematical Sciences*. Springer, Berlin, Heidelberg, New York, 1988-1993.

[18] B. Eckhardt, J. Ford, and F. Vivaldi. Analytically solvable dynamical systems which are not integrable. *Physica D: Nonlinear Phenomena*, 13(3):339–356, November 1984.

[19] J. P. Eckmann and D. Ruelle. Ergodic theory of chaos and strange attractors. *Reviews of Modern Physics*, 57(3):617–656, July 1985.

[20] S. Gouezel. Central limit theorem and stable laws for intermittent maps. *Probability Theory and Related Fields*, 128(1):82–122, January 2004.

[21] E. Gutkin. Billiards in polygons. *Physica D: Nonlinear Phenomena*, 19(3):311–333, April 1986.

[22] E. Gutkin. Billiards in polygons: Survey of recent results. *Journal of Statistical Physics*, 83(1-2):7–26, April 1996.

[23] E. Gutkin. Billiard dynamics: An updated survey with the emphasis on open problems. *Chaos: An Interdisciplinary Journal of Nonlinear Science*, 22(2):026116, June 2012.

[24] E. Gutkin and A. Katok. Weakly mixing billiards. In *Holomorphic Dynamics*, pages 163–176. Springer Berlin Heidelberg, 1988.

[25] D. Hansel, G. Mato, and C. Meunier. Clustering and slow switching in globally coupled phase oscillators. *Physical Review E*, 48(5):3470–3477, November 1993.

[26] M. Horvat, M. D. Esposti, S. Isola, T. Prosen, and L. Bunimovich. On ergodic and mixing properties of the triangle map. *Physica D: Nonlinear Phenomena*, 238(4):395–415, March 2009.

[27] J. Huang and H. Zhao. Ultraslow diffusion and weak ergodicity breaking in right triangular billiards. *Physical Review E*, 95(3):032209, March 2017.

[28] S. G. Johnson and M. Frigo. Fastest fourier transform in the west, 2003.

[29] A. Katok. Interval exchange transformations and some special flows are not mixing. *Israel Journal of Mathematics*, 35(4):301–310, December 1980.

[30] M. Keane. Interval exchange transformations. *Mathematische Zeitschrift*, 141:25–32, 1975.

[31] R. Kenyon and J. Smillie. Billiards on rational-angled triangles. *Commentarii Mathematici Helvetici*, 75(1):65–108, April 2000.

[32] S. Kerckhoff, H. Masur, and J. Smillie. Ergodicity of Billiard Flows and Quadratic Differentials. *The Annals of Mathematics*, 124(2):293, September 1986.

[33] R. Klages, G. Radons, and I. M. Sokolov, editors. *Anomalous Transport: Foundations and Applications*. Wiley-VCH, July 2008.

[34] A. Klenke. *Probability Theory*. Springer Berlin, 2006.

[35] M. Krupa. Robust heteroclinic cycles. *Journal of Nonlinear Science*, 7(2):129–176, April 1997.

[36] T. Araújo Lima, S. Rodríguez-Pérez, and F. M. de Aguiar. Ergodicity and quantum correlations in irrational triangular billiards. *Physical Review E*, 87(6), June 2013.

[37] Č. Lozej, G. Casati, and T. Prosen. Quantum chaos in triangular billiards. *Physical Review Research*, 4(1):013138, February 2022.

[38] H. Masur and S. Tabachnikov. Rational billiards and flat structures. In *Handbook of dynamical systems, Vol. 1A*, pages 1015–1089. North-Holland, Amsterdam, 2002.

[39] J.-Ch. Puchta. On triangular billiards. *Commentarii Mathematici Helvetici*,

76(3):501–505, September 2001.

[40] P. J. Richens and M. V. Berry. Pseudointegrable systems in classical and quantum mechanics. *Physica D: Nonlinear Phenomena*, 2(3):495–512, June 1981.

[41] R. E. Schwartz. Obtuse triangular billiards II: One hundred degrees worth of periodic trajectories. *Experimental Mathematics*, 18(2):137–171, January 2009.

[42] J. Seaward. Ergodicity in golden billiards. *arXiv e-prints*, 2019.

[43] A. Shudo. Length spectrum and semiclassical density of states for an almost-integrable billiard system. *Physical Review A*, 46(2):809–824, July 1992.

[44] Y. A. G. Sinai and C. Ulcigrai. Weak mixing in interval exchange transformations of periodic type. *Letters in Mathematical Physics*, 74(2):111–133, November 2005.

[45] J. Slipantschuk, M. Richter, D. J. Chappell, G. Tanner, W. Just, and O. F. Bandtlow. Transfer operator approach to ray-tracing in circular domains. *Nonlinearity*, 33(11), September 2019.

[46] G. Tanner. Dynamical energy analysis—determining wave energy distributions in vibro-acoustical structures in the high-frequency regime. *Journal of Sound and Vibration*, 320(4-5):1023–1038, March 2009.

[47] J. L. Varona. Rational values of the arccosine function. *Central European Journal of Mathematics*, 4:319–322, June 2006.

[48] W. A. Veech. Teichmuller curves in moduli space, eisenstein series and an application to triangular billiards. *Inventiones Mathematicae*, 97(3):553–583, October 1989.

[49] M. Viana. Ergodic theory of interval exchange maps. *Revista Matemática Complutense*, 19(1), April 2006.

[50] Ya B. Vorobets. Ergodicity of billiards in polygons: explicit examples. *Russian Mathematical Surveys*, 51(4):756–757, August 1996.

[51] Ya B Vorobets. Ergodicity of billiards in polygons. *Sbornik Mathematics*, 1997.

[52] P. Walters. *An Introduction to Ergodic Theory*. Springer New York, October 2000.

[53] J. Wang, G. Casati, and T. Prosen. Nonergodicity and localization of invariant measure for two colliding masses. *Physical Review E*, 89(4), April 2014.

[54] K. Zahradova, J. Slipantschuk, O. F. Bandtlow, and W. Just. Impact of symme-

try on ergodic properties of triangular billiards. *Physical Review E*, 105:L012201, January 2022.

[55] A. N. Zemlyakov and A. B. Katok. Topological transitivity of billiards in polygons. *Mathematical Notes of the Academy of Sciences of the USSR*, 18(2):760–764, August 1975.